The experimental and theoretical investigation of single-crystal diamond compound refractive lenses (CRLs)

by

Qiuyuan Zhang

Thesis submitted in fulfilment of
the requirements for the degree of
PHILOSOPHIAE DOCTOR
(PhD)

Faculty of Science and Technology
Department of Mathematics and Physics
2020

University of Stavanger
NO-4036 Stavanger
NORWAY
www.uis.no

ISBN: 978-82-7644-934-1
ISSN:1890-1387
PhD: Thesis UiS No. 527

Acknowledgements

The research work was carried out from November, 2015 to January, 2020 at the Department of Mathematics and Physics, Faculty of Science, University of Stavanger, Norway. We acknowledge that the PhD project is fully financed by the Norwegian Ministry of Education and the University of Stavanger.

First and foremost, I would like to express my deepest appreciation to my main supervisor - Prof. **Helge Bøvik Larsen** for his valuable and constructive suggestions during the planning and development of my PhD project in the past four years. There is no exaggeration to say that his selfless support is the prerequisite for the completion of the doctoral thesis. Not only has he cultivated my ability to think independently, but also has given me useful guidance from his professional perspective. Besides, I would like to express my sincere gratitude to my co-supervisor - Prof. **Gunnar Thorkildsen** for his expertise and immense patience in guiding my research, especially in extracting useful information from the effective diffraction patterns and completing the procedure to compute the **UB** matrix in Wolfram Mathematica 11.0.

Secondly, I feel really grateful to the leader of our department – Bjørn Henrik Auestad and other helpful colleagues, especially Stian Ramsnes, Mark Bogers, Giorgio Pattarini, Matthew Terje Aadne and Abhijit Bhat Kademane, *etc*.

Thirdly, I am indebted to the ESRF committee for providing valuable beam time at the BM31 station, one of the Swiss-Norwegian beamlines (SNBL) at European Synchrotron Radiation Facility (ESRF), France. Besides, I would also acknowledge the help from the beamline scientist of BM31 station - Hermann Emerich, Dr. Maxim Polikarpov from EMBL, Prof. Ragnvald Mathiesen (NTNU), Nataliya Klimova (IKBFU), Prof. Snigirev Anatoly (IKBFU) and Irina Snigireva (ESRF).

Last but not least, I really want to extend my appreciations to my parents, my beloved wife and lovely daughter, for their tremendous support and encouragement throughout this period.

Qiuyuan Zhang

Stavanger, Norway, February 2020

Summary

In the field of X-ray optics, compound refractive lenses (usually termed CRLs) function as a focusing device for hard X-rays and they are believed to possess a lot of prominent advantages over other focusing devices, such as the ease of alignment and compactness. Among all the potential materials used to fabricate CRLs, diamond stands out mainly due to its unique physical properties, *e.g.* strong thermal resistance and the ability to keep stable under extremely intense radiation (suitable for the even brighter next-generation X-ray source). When choosing between single-crystal and polycrystalline diamond, single-crystal diamond is favoured because it can avoid unwanted diffuse scattering induced by a sintered structure of polycrystalline diamond. Therefore, single-crystal diamond CRLs deserve a comprehensive analysis and are chosen as the subject of this thesis.

This PhD thesis consists of seven chapters. Chapter 1 reviews the history of two different kinds of X-ray sources, conventional X-ray tubes and synchrotron radiation (SR) light sources, including their principles of operation and the novel development of SR sources. Followed by that, Chapter 2 primarily focuses on X-ray optical devices and more emphasis is given to the X-ray beam conditioning devices (including both monochromators and X-ray focusing elements). Among a variety of focusing devices, CRLs turn out to be a huge success since the invention in 1990s and have been investigated in the aspect of focusing effect. However, a phenomenon that several significant intensity drops have been captured in the energy spectrum and are vividly termed as 'glitch effects', which call for a more rigorous treatment both experimentally and theoretically. Chapter 3 gives an overview of two experimental setups at BM31 (ESRF), France. As a good starting point, an energy scan was set up to investigate the influence of some possible experimental features on the glitches while sweeping through a range of photon energies, namely, the beam divergence, χ-angle of the goniometer and

different scanning positions. Besides, the energy spectrum also serves as a good reference for the second experiment, which was set up under almost the same configuration so that we can compare our simulation with the retrieved energy spectrum. The glitches appearing in the spectrum are mainly contributed by Bragg diffraction, which is strongly dependent on the orientation of single–crystal diamond. Then the major task became the prediction of both the 'strengths' and positions of glitches, and the established ω-scan setup was to calculate the misalignment of the single crystal with respect to the assumed ideal beam direction. This is usually achieved via the orientation matrix by analysing the collected diffraction patterns. In this sense, the latter ω-scan is regarded as a continuation of the former energy scan. The experimental results, together with the theoretical investigation on the basis of orientation matrix, form the backbone of the current thesis. Chapter 4 mainly discusses the intensity distribution on the exit surface of a single 2D diamond half lens in the symmetrical Laue case using an X-ray lab source because it may provide useful hints when one want to deal with a more complicated case - biconcave lenses. This chapter includes both detailed theoretical derivations and the corresponding simulations. The intensity distribution on the exit surface is studied provided that a certain type of Bragg reflection occurs. Additionally, this is achieved by replacing the curved parabolic entrance with a bunch of staircase crystals with various thickness. Chapter 5 lists all the publications during the PhD period. Chapter 6 wraps up the whole project and points out some possible applications based on the research results. Furthermore, we specify some possible subjects of future investigations. An outline of some other contributions I have made is given in Chapter 7. In the end of this thesis, one can refer to Appendices for the wavelength calibration process and the procedure on how to calculate the orientation matrix in two different cases.

List of publications

(1) Zhang, Q., Polikarpov, M., Klimova, N., Larsen, H.B., Mathiesen, R., Emerich, H., Thorkildsen, G., Snigireva, I. and Snigirev, A., 2019. Investigation of 'glitches' in the energy spectrum induced by single-crystal diamond compound X-ray refractive lenses. *Journal of synchrotron radiation*, **26**(1), pp.109-118.

(2) Zhang, Q., Polikarpov, M., Klimova, N., Larsen, H.B., Mathiesen, R., Emerich, H., Thorkildsen, G., Snigireva, I. and Snigirev, A., 2019, January. Investigation of glitches induced by single-crystal diamond compound refractive lenses based on crystal orientation. *AIP Conference Proceedings* (Vol. **2054**, No. 1, p. 060007). AIP Publishing LLC.

(3) Zhang, Q. and Larsen, H.B., 2020 (to be submitted). Investigation of single-crystal diamond 2D half lens in symmetrical Laue case.

List of conference presentations and posters

(1) Zhang, Qiuyuan; Polikarpov, Maxim; Klimova, Nataliya; Larsen, Helge Bøvik; Mathiesen, Ragnvald; Emerich, Hermann; Snigireva, Irina; Snigirev, Anatoly (2018). Investigation of glitches induced by single-crystal diamond compound refractive lenses. International Conference on Synchrotron Radiation Instrumentation (SRI 2018). June 10-15, 2018, Taipei, Taiwan. Poster presentation. *Event link:*

http://sri2018.nsrrc.org.tw/

(2) Zhang, Qiuyuan; Polikarpov, Maxim; Klimova, Nataliya; Larsen, Helge Bøvik; Mathiesen, Ragnvald; Emerich, Hermann; Snigireva, Irina; Snigirev, Anatoly (2018). Glitch spectroscopy of X-ray compound refractive lenses. ESRF user meeting. February 5-7, 2018, Grenoble, France. Oral presentation & poster presentation. *Event link:*

https://www.esrf.eu/fr/home/events/conferences/2018/user-meeting-2018.html

Table of Contents

Table of Figures

List of Tables

Appendices

1 Introduction

1.1 *The nature of X-rays*

In 1895, the Nobel Prize-winning scientist Wilhelm Röntgen discovered a type of radiation with a lot of peculiar properties and simply named it "X-ray radiation" to signify its unknown nature. To honour his outstanding contribution, X-ray radiation is also called "Röntgen radiation". At that time, the lack of understanding of its nature did not hinder X-ray's rapid application and it was soon used to detect the internal structure of materials owing to its very strong penetrating ability. It was not until 1912 when Max von Laue proposed in a conversation with Paul Peter Ewald that X-rays should be diffracted, if a crystal indeed were constructed like 3D periodic lattices with the inter-atomic distance of 0.5-2.5Å, which should be in the same order of the wavelength of the incident X-ray radiation. In other words, the crystal forms an ideal optical grating for X-rays. To verify this idea, he set up an experiment with the help of two experienced X-ray experimentalists - Friedrich and Knipping like this: an X-ray beam was confined to go through a cooper sulfate crystal and a photographic plate was placed right after the sample to record the result. It was shown on the plate that a central spot induced by the primary transmitted beam was surrounded by a cluster of diffraction spots. In fact, the experiment justified two facts at the same time: the wave nature of X-rays and the periodic lattice structure of the crystal. Two years later, Laue was also awarded the Nobel Prize in Physics for his tremendous contributions to X-ray diffraction theory. For a more detailed description of X-ray's historical development, the recent paper by Authier [1] should be consulted.

Within X-rays' regime, the scientists further classify into two categories according to the penetrating ability: hard X-rays ($\lesssim 2$Å) and soft X-rays (> 2Å). Literally, hard X-rays can penetrate through relatively thicker objects without losing much intensity and are often used to perform

crystallographic analysis and non-destructive detection; whereas the scientists are able to use soft X-rays to see extremely small features of the sample.

The mechanism underlying X-rays' numerous applications is based on the interaction of light with the matter and Fig. 1 shows the physical phenomena that may occur when an X-ray beam illuminates a sample.

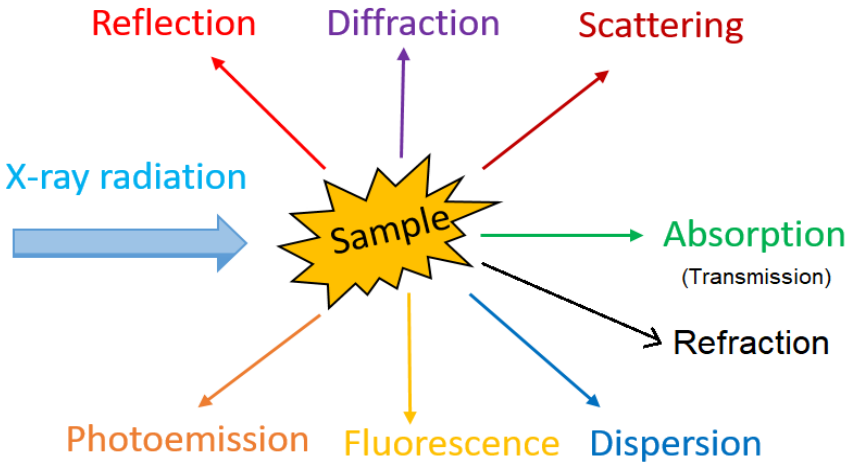

Figure 1 – A variety of physical phenomena when shining X-ray radiation onto a sample.

1.1.1 The wave nature of X-rays

Since X-rays are a kind of electromagnetic waves, they certainly display wave nature. The electric field vector and magnetic field vector are always perpendicular to each other, and both lie in the plane perpendicular to the propagation direction of X-rays. As is depicted in Fig. 2, for unpolarized X-rays, the electric $\boldsymbol{E}$ and the magnetic field vector $\boldsymbol{H}$ can point to any direction within yOz plane, but they are still perpendicular to each other; a special case is if the electric field of X-rays is confined to xOy plane, they are so-called plane waves.

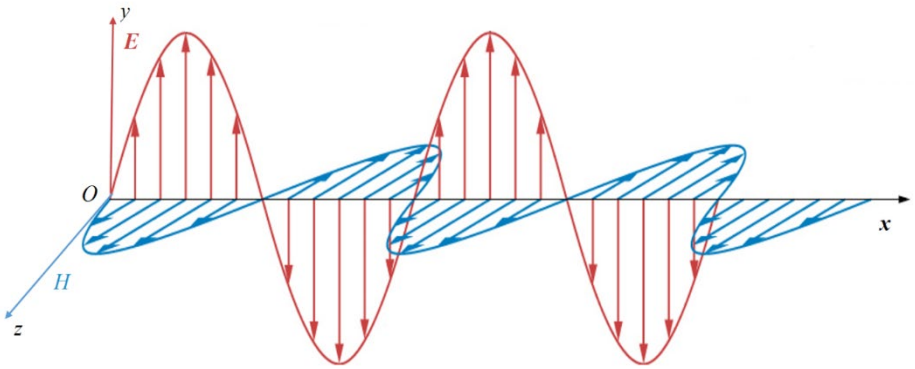

Figure 2 – The relationship between the electrical field and the magnetic field of a plane wave.

In the classical theory, electromagnetic waves can give rise to a series of different phenomena, such as refraction, reflection, scattering, interference and diffraction, so do X-rays.

1.1.2 The particle nature of X-rays

In the light of quantum theory, the electromagnetic wave is considered as a kind of particle flow composed of light quanta or photons. Therefore, X-rays possess the same wave-particle duality as other electromagnetic waves. For each photon with the energy ε in the unit of keV and momentum p, the following relations are satisfied:

$$\begin{cases} \varepsilon[\text{keV}] = h\upsilon = h\dfrac{c}{\lambda} = \dfrac{12.398}{\lambda[\text{Å}]} \\ p = \dfrac{h}{\lambda} \end{cases}$$

In this equation, h is Planck constant, υ is the frequency, c is the speed of light and λ is the wavelength.

Due to the particle characteristics of X-rays, the photons can only be absorbed or re-emitted entirely when exchanging energy with the matter.

In a word, the wave-particle duality is the objective attribute of X-rays. One should note that under certain conditions, it is possible that only one aspect may behave more obviously; however, when the condition changes, the other aspect may be observed.

1.2 *X-ray sources*

By now, several mechanisms have been employed to produce X-rays, for instance, electronic process (X-ray tubes), synchrotron radiation (SR) or free electron lasers (FEL). In this thesis, we focus primarily on synchrotron radiation facilities since they are commonly used nowadays. Moreover, the novel development of SR will also be briefly introduced.

It is known that an ideal point source can be described by measuring the radiant flux within a small solid angle, but it is not applied for synchrotron radiation because it is seen as a complex light source ranging from infrared to hard X-rays. In order to evaluate X-ray sources, especially SR, a bunch of factors should be taken into account, they are the number of photons produced per second, the angular divergence, the cross-section of the beam and the photons falling within a bandwidth of 0.1% of the central frequency ω, respectively. These four factors together, define the brilliance (also called spectral brightness) of synchrotron radiation and the resulting unit is denoted as $\mathrm{photons/(s \cdot mm^2 \cdot mrad^2 \cdot 0.1\%BW)}$. In other words, "brilliance" is a term that describes both the brightness and the angular spread of the beam and greater brilliance means more photons of a given wavelength and direction are concentrated on a spot per unit of time. That is why brilliance is a common beam characteristic when comparing different X-ray sources and Fig. 3 shows how the brilliances of various X-ray sources are increasing with the time.

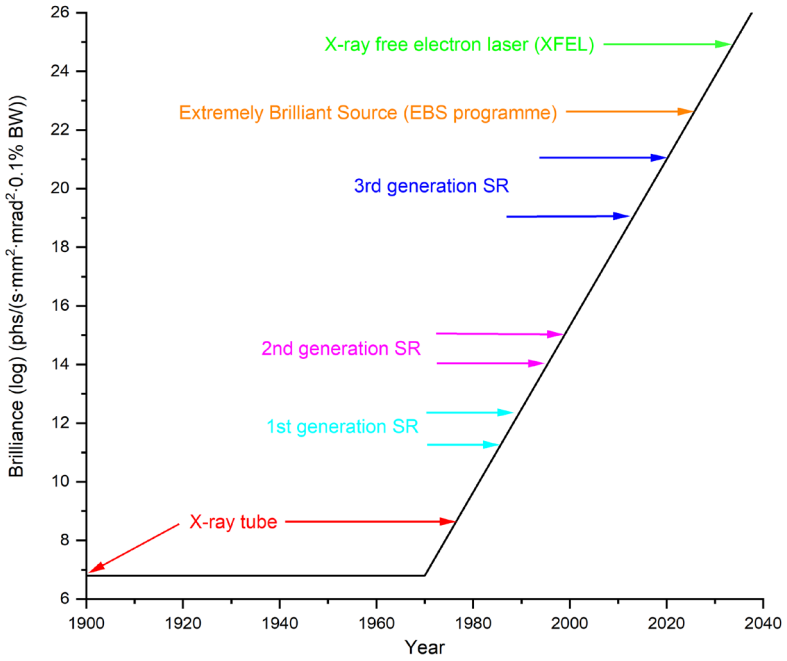

Figure 3 – The brilliances of different X-ray sources as a function of years (reproduced from https://www.esrf.eu).

In addition, another commonly used parameter is the flux, which is defined as the number of photons emitted by the X-ray source per second per 0.1%BW (photons/(s · 0.1%BW)). This parameter will be used in the following simulations because it may also evaluate the quality of the generated radiation.

1.2.1 Conventional X-ray tubes

The X-ray tube is the simplest and most versatile X-ray source and has been widely used in various X-ray instruments, such as CT scanners, airport luggage scanners, X-ray crystallography, material and structure analysis.

An X-ray tube is a controllable source and the fundamental principle is: when a bunch of high speed electrons in the X-ray tube bombard the anode, their motions change immediately, thereby generating electromagnetic waves. Based on the quantum physics theory, when electrons collide with atoms of the anode target, the electrons lose energies after colliding with the atoms constituting the anode, and the loss of energy is radiated in the form of photons. During the entire process, some of these electrons may exhaust whole energy after a single process and this leads to the radiation having the maximum frequency, while most electrons have to undergo multiple collisions before their energies are totally consumed. As a result, in addition to the continuous spectrum ("Bremsstrahlung" in German, *i.e.*, "brake radiation"), there exist two discrete characteristic lines (K_α and K_β radiation), which result from the decay of excited states of the element of the tube. For a given target, the characteristic spectral wavelength has a certain value and change of the tube voltage and current can only affect the intensity of the spectrum. One should note that only when the tube voltage is above the critical voltage (referred to as "excitation voltage"), characteristic lines may appear on the basis of a continuous spectrum.

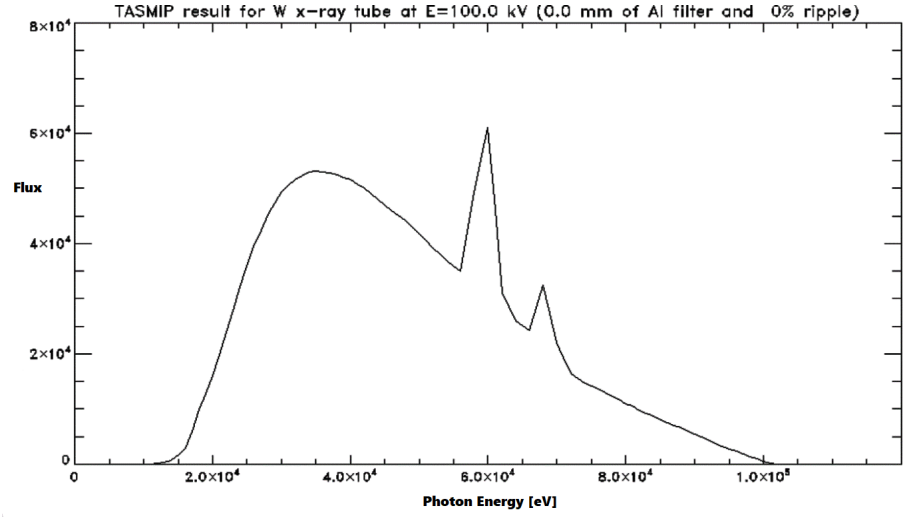

Figure 4 – The flux of a tungsten X-ray tube.

This explains why the emitted spectrum is a superposition of a continuous spectrum and characteristic lines, as is shown in Fig. 4. Therefore, the radiation produced by an X-ray tube is completely unpolarized and can be considered as a collection of incoherent point sources which can generate incoherent spherical waves. This is a very useful assumption and will be used in our simulations (Chapter 4).

However, for X-ray tubes, only a very small portion of electrical input power (1%) is converted into X-rays, and the remaining into heat. Therefore, heat dissipation is an issue of great concern and many efforts have already been made. According to different heat dissipation methods, X-ray tubes can be further classified into two kinds, the sealed tube and rotating anode, respectively. As their names indicate, the anode of the sealed tube is stationary with water being employed as a coolant, while the other aims to improve the efficiency of heat dissipation by rotating the anode at a high speed (3000 to 9000 rpm). It turns out that the output power of a rotating anode tube can reach up to 120 kW and is much higher than that of a sealed tube (in the order of 1 kW). In consequence, we can come to the conclusion that heat dissipation efficiency affects the output power significantly.

1.2.2 Synchrotron radiation (SR)

Apart from conventional X-ray tubes, synchrotron radiation is treated as an irreplaceable X-ray source and has greatly pushed forward the boundaries of basic research and high-tech applications owing to many fascinating features. With the increase of energy in the storage rings, the wavelength of the synchrotron radiations shifts from ultraviolet, soft X-rays to the range of hard X-rays. In other words, the SR facility is a comprehensive light source with a rather wide spectrum.

Rigorously speaking, the scientific definition of synchrotron radiation is electromagnetic radiation emitted by a relativistic charged particle when it moves along a circular orbit under the influence of a magnetic field.

As a matter of fact, two conditions should be fulfilled simultaneously to produce synchrotron radiation: one is a charged particle travelling at a high speed that is comparable to that of light; the other is existence of a magnetic field that changes the motion of the charged particles. In principle, all charged particles (such as electrons, positrons and ions) can be injected into the storage rings. However, electrons are exclusively used in practical situation because they are easily attainable using an electron gun and it takes much less energy to accelerate them compared with other heavier ions.

Before synchrotron radiation was discovered, it is already known that that high-speed electrons emit radiation when their velocities change. In 1873, Maxwell proved that the variation of charge density and circuit can radiate electromagnetic waves; 14 years later, Hertz proved the existence of the electromagnetic wave in 1887, which formed a complicated theoretical basis for synchrotron radiation; in 1897, Sir Joseph Larmor derived an expression from classical electrodynamics for the power radiated by an accelerated charged particle; only one year later, A. Liénard derived the equation of radiated power by the electrons undergoing centripetal acceleration in a circular trajectory. Followed by that, Schott gave the expressions for the angular distribution of the radiation as a function of the harmonic of the orbital frequency in 1907. In 1940s, the synchrotron radiation became a reality. D. Iwanenko and I. Pomeranchuk [2] made predictions of synchrotron radiation in 1944, and the first indirect observation of synchrotron radiation (SR) was made by Blewett [3] in 1945. The year of 1947 witnessed a milestone in the history of artificial light sources - synchrotron radiation was visually observed for the first time at the 70-MeV synchrotron source of General Electric Company (GE) (Fig. 5) in Chicago, USA.

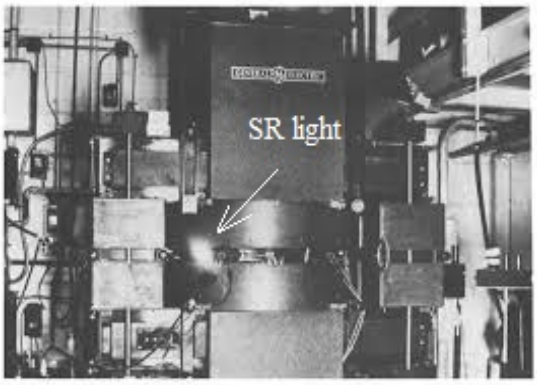

Figure 5 – A 70-MeV synchrotron source built by General Electric Company (GE) [4].

The systematic theory on the emission of electromagnetic radiation by a charged particle moving along a circular orbit at relativistic velocity was proposed by Julian Schwinger [5] in 1949. In 1956, early utilization of synchrotron radiation was achieved by D. H. Tomboulian [6] at 300 MeV Cornell Synchrotron at Cornell University. In 1965, SR utilization started at DESY, Germany. In 1968, the first SR light source ("Tantalus") was constructed at Wisconsin University and it was actually converted from a colliding machine prototype to SR light source, namely, parasitic use. It was soon realized that the first-generation synchrotron radiation was a comprehensive light source with excellent performance, but was severely constrained by the original design. To make full use of this excellent source, the second-generation radiation source (also known as "bending magnet") started to appear in late 1970s and it was considered as a dedicated source because it no longer served for high-energy physics experiments. As time went by, the current SR facilities could not meet the increasing demands for higher quality X-rays and this led to the advent of optimized SR sources by introducing the so-called "insertion devices". In fact, the insertion devices are periodic magnetic arrays which force the injecting electrons to move on sinusoidal or elliptical trajectories. In 1990s, quite a few large third-generation sources began to spring up worldwide, among which the European Synchrotron Radiation Facility (ESRF) in France, Advanced

Photon Source (APS) in the USA and SPring-8 synchrotrons in Japan were three typical examples and some of their key parameters are listed in Table 1.

Table 1 – Some parameters of the above mentioned SR sources: ESRF, APS and Spring-8.

SR source	**Energy (GeV)**	**Current (mA)**	**Circumference (m)**	**Emittance (nm.rad)**	**Straight section (m)**
ESRF	6.0	200	844.4	3.7	32×6.3
APS	7.0	100	1104	3.0	40×6.7
SPring-8	8.0	100	1436	2.8	44×6.4, 4×30

The third-generation synchrotron sources were constructed with long straight sections to house the insertion devices (wigglers and undulators) to maximize the intensity of the generated radiation. One should note that the spectrum of wigglers is similar to that of a bending magnet but with higher brilliance, and the wavelength of the radiation is shifted towards the shorter wavelength. This is owing to alternating polarity of several dipole magnets and the total beam can be regarded as an incoherent sum of each independent beam emitted by the dipoles. Nevertheless, when it comes to the undulator scheme, the beam is considered as a coherent sum due to the periodic structure of dipole magnets. By comparing these two types of insertion devices, we find that undulators can deliver a narrower radiation cone with a more intense beam by using smaller and lower field bending and selected wavelengths, or alternatively, harmonics can be tuned by manipulating the magnetic field of the device by means of changing the gap. Fig. 6 depicts three different mechanisms of producing

SR (bending magnet, wiggler and undulator) and Fig. 7 shows their corresponding flux versus photon energy by using XOP 2.4 [7].

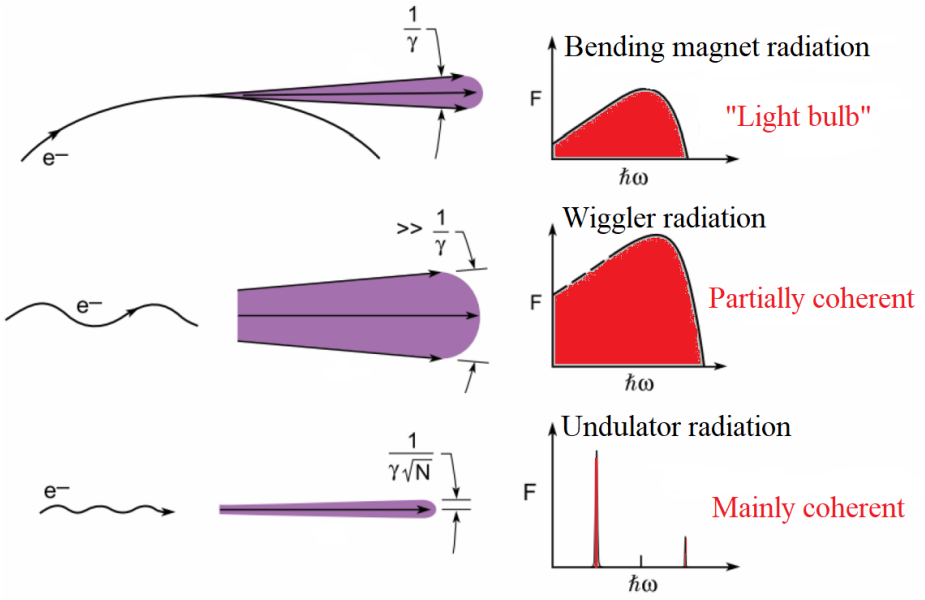

Figure 6 – The flux (F) of synchrotron radiation produced by three different mechanisms. $\gamma = E/mc^2$ and equals $1957E$[GeV] for electrons and N is the number of magnetic periods.

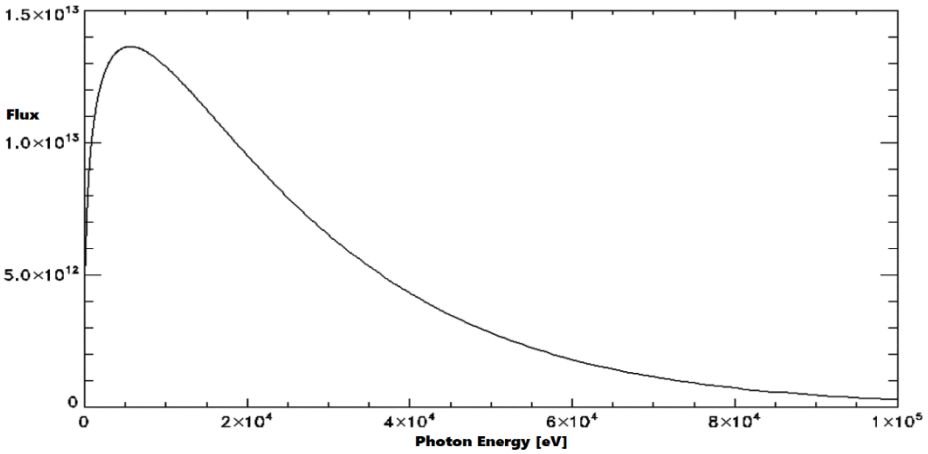

(a) the flux of a bending magnet (cone radiation).

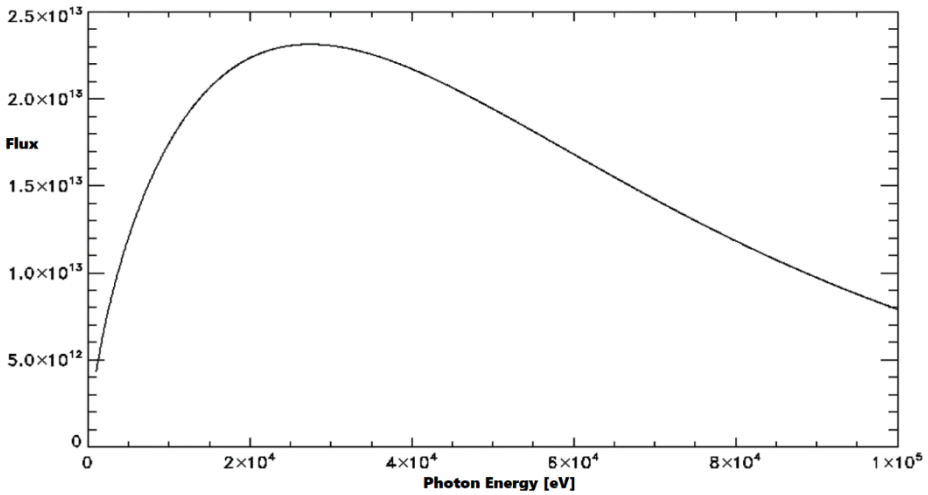

(b) the flux of a wiggler.

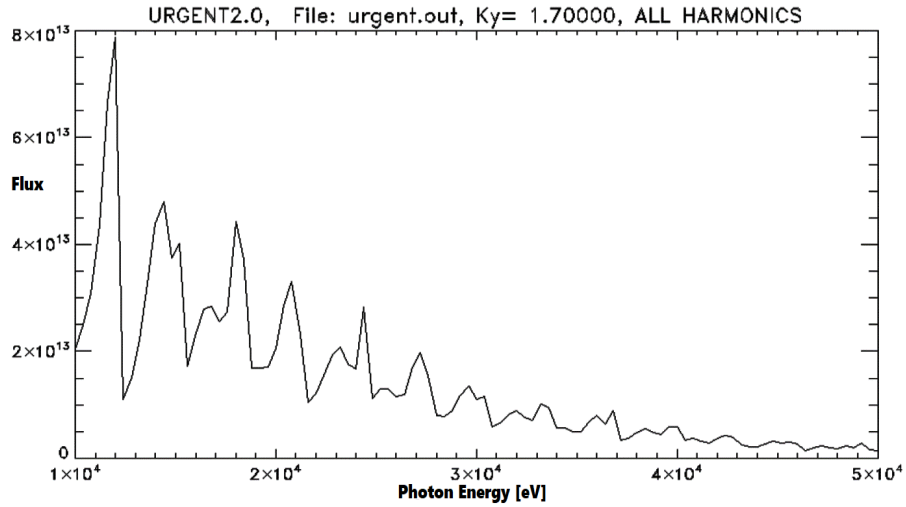

(c) the flux of an undulator.

Figure 7 – The flux of synchrotron radiation produced under three different mechanisms; (a) the flux of a bending magnet, (b) the flux of a wiggler and (c) the flux of an undulator.

In order to make the readers have an intuitive understanding of the internal structure of synchrotron radiation facility, we simply choose ESRF as an example given in Fig. 8.

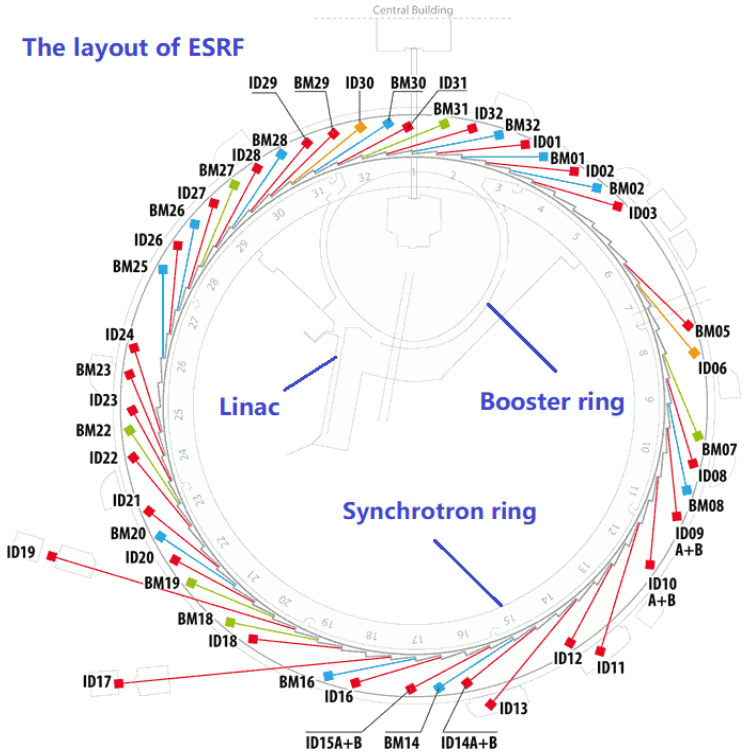

Figure 8 – A schematic drawing of ESRF (before the upgrade programme-EBS) labelled with some key elements. Note that BM denotes the beamline generated under a bending magnet mechanism, while ID denotes that produced by the undulator (reproduced from https://www.esrf.eu and has been modified).

In general, four key components make up a complete synchrotron facility: a linear accelerator (LINAC), a booster ring, a synchrotron ring, synchrotron radiation beamlines and their affiliated experimental workstations. The LINAC is used to accelerate the electrons to 20000 keV before being injected into the booster ring; a booster ring is where the electrons are accelerated up to the order of GeV (for instance, the energy of ESRF storage ring is 6 GeV); a storage ring in which the electrons are further accelerated close to the speed of light and X-rays are then produced tangential to the plane of orbit. To make full use of this valuable resource, the synchrotron elicited from a storage ring is

filled in the experimental hall and the scientists from different groups are able to perform a variety of experiments at the same time.

The notable characteristics of synchrotron radiation are summarized here:

(1) Extremely high brilliance; as has been demonstrated in Fig. 3, the brilliance of SR facilities is more than a billion times higher than laboratory X-ray tubes. Brilliance is a term that describes both the brightness and the angular spread of the beam. Higher brilliance makes it possible to see more detail in the material under investigation. That is why the request for increased brilliance is so crucial.

(2) A wide and tunable spectrum; SR generated by both bending magnets and wigglers has a wide and continuous spectrum within X-ray's range, by contrast, the radiation emitted by the undulator can be seen as sharp quasi-monochromatic peaks.

(3) Pulsed time structure in the order of nanoseconds; a relativistic electron is usually characterized by the following relativistic factor $\gamma = \frac{1}{\sqrt{1-\left(\frac{v}{c}\right)^2}} = \frac{1}{\sqrt{1-\beta^2}}$, where β is the factor of velocity v normalized by the speed of light in vacuum c ($\beta = \frac{v}{c}$). The Lorentz force for a relativistic electron in a constant magnetic field is given:

$$\mathbf{F} = \frac{d\mathbf{P}}{dt} = -e\mathbf{v} \times \mathbf{B} \tag{1.1}$$

where $\mathbf{P} = \gamma m\mathbf{v}$, $\mathbf{B}$ is the magnetic field.
In a constant magnetic field, the change rate of the electron's energy should be equal to 0, namely,

$$\frac{dE_e}{dt} = \mathbf{v} \cdot \mathbf{F} = -e\mathbf{v} \cdot (\mathbf{v} \times \mathbf{B}) \equiv 0 \tag{1.2}$$

By substituting $E_e = \gamma mc^2$ into above Eqn. (1.2), we can obtain

$$\frac{dE_e}{dt} = \frac{d}{dt}(\gamma \mathrm{m}c^2) = 0 \tag{1.3}$$

It can be inferred that $\gamma = \text{constant}$ and the force equation in (1.1) becomes:

$$\mathbf{F} = \frac{d\mathbf{P}}{dt} = \gamma \mathrm{m} \frac{d\mathbf{v}}{dt} = -e\mathbf{v} \times \mathbf{B} \tag{1.4}$$

By rewriting the equation in the scalar form as:

$$\gamma \mathrm{m}(\frac{-v^2}{R}) = -evB \tag{1.5}$$

with $B = \frac{\mathrm{m}\gamma c}{Re}$ and R being the radius of the orbit.

The duration of the radiation pulse is equal to the time difference between the time required for the electron to pass through the arc and for the light to go through its corresponding chord. The duration of the radiation pulse is thus denoted as:

$$\Delta t = \frac{\text{arc length}}{v} - \frac{\text{chord length}}{c} \approx \frac{R \cdot 2\theta}{v} - \frac{2R \cdot \sin\theta}{c} \tag{1.6}$$

The two approximations of $\theta \approx \frac{1}{2\gamma}$ and $\sin\theta \approx \theta$ are applied here due to the smallness of θ angle. Then by substituting $v = \beta c$ into the above equation, we can deduce the duration of the pulse as:

$$\Delta t \approx \frac{R}{\gamma \beta c}(1 - \beta) \tag{1.7}$$

By substituting $(1 - \beta) \approx \frac{1}{2\gamma^2}$ and $R \approx \frac{\gamma mc}{eB}$ into Eqn. (1.7), it is transformed into:

$$\Delta t \approx \frac{\mathrm{m}}{2eB\gamma^2} \tag{1.8}$$

By substituting the values for electrons, the duration the pulse is between 0.01-1 nanosecond or even shorter.

(4) Low emittance as a result of the smallness of both the source size and angular distribution of the beam; the emittance of the synchrotron radiation, ϵ, which is defined as the product of both the horizontal and vertical emittance. It is known that the intensity is inversely proportional to the cross section area of the beam, a small extension in space means large intensity and is desirable. For the second-generation SR, the emittance is of the order of several hundred nm rad, but the emittance of the third-generation SR sources is significantly reduced to 5-20 nm rad.

(5) A high level of polarization; the radiation is plane polarized in the plane of orbit. As the direction of observation deviates from the plane of the orbit, the radiation becomes elliptically polarized. Recently, a planar undulator [8] has been designed to generate variably polarized radiation and a helical undulator [9] has been employed to produce circularly polarized radiation.

(6) High coherence due to the smallness of the source size and very long source-to-sample distance in the third-generation facilities; coherence is another key parameter that reflects the degree to which SR can produce detectable wave-like effects like diffraction and interference. Good coherence allows to observe very weak perturbations of X-ray's wavefront and turns out to be useful in some practical techniques, in particular, phase contrast imaging [10]. It becomes a reality that coherence-enhanced SR sources have been built and it is important to note that coherence includes both temporal (or longitudinal) and spatial (or lateral) coherence. Temporal coherence usually refers to the coherence of the electromagnetic disturbances at two points along the propagation direction and can be characterized by the coherence length. In fact, temporal coherence is usually achieved simply by making the beam monochromatic with a common optical device called "monochromator", which will be introduced in detail in the following chapter and it is thus estimated by the energy resolution of the monochromator ($\Delta\lambda/\lambda$). Correspondingly, spatial or lateral coherence refers to the disturbance perpendicular to the propagation direction and is described by the spatial extension Δy of the beam (Fig. 9).
Here we assume two emitting point sources with Δy apart for illustration and the condition for coherence is then given by $\Delta y \cdot \Omega_y < 2\lambda$, where $\Omega_y = d/D$. Since the sample-to-detector for synchrotron facilities may reach more than one hundred meters, it may significantly decrease Ω_y and thus has a positive effect on the increase of spatial coherence.

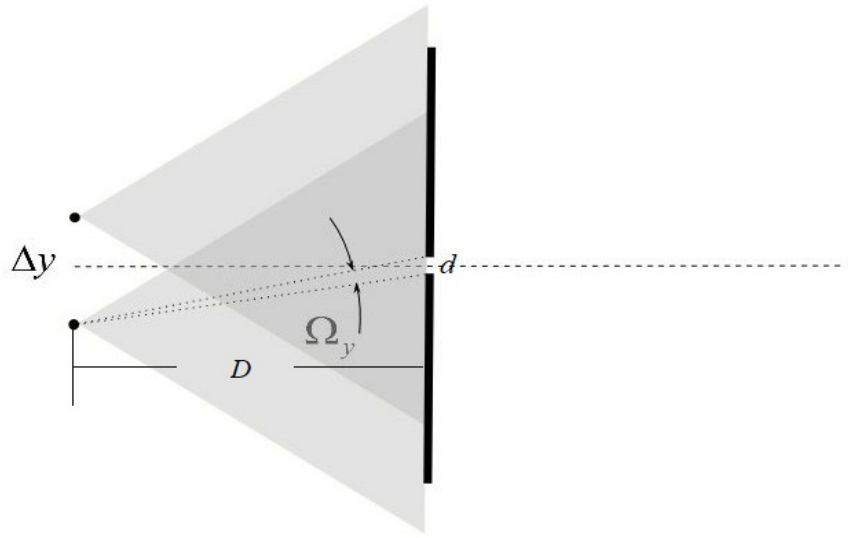

Figure 9 – Definition of spatial coherence (http://photon-science.desy.de).

1.3 *Current development of synchrotron radiation*

In spite of these prominent features that the current synchrotron radiation facilities possess, the scientists are still in pursue of delivering even higher quality beams. The ESRF, as a pioneer in synchrotron radiation and synchrotron-based technologies, launched an ambitious upgrade programme - the Extremely Brilliant Source (EBS) in 2015 to maintain its lead in this field. The main focus of EBS project is the design and implementation of a new low-emittance storage ring to be built in the existing tunnel and the brilliance of the upgraded synchrotron ring is expected to be at least 100 times more brilliant than the current one. In addition, this programme also involves in constructing four brand new EBS flagship beamlines and refurbishing three existed beamlines. In addition, new platforms of cryo-EM (for structure determination purpose of biological macromolecules without crystallization) and high-power laser facility (for the purpose of creating exotic states of the sample at ultra-high temperatures and pressures) will be developed, conducting currently unavailable experiments. In parallel, proper exploiting the

EBS's outstanding X-ray properties calls for advanced instrumentation, such as more powerful detector systems and robust X-ray optical devices. Besides, data processing efficiency should be enhanced, which includes real-time data visualization, data storage and rapid data processing.

However, the well-planned upgrade projects is still not counted as a cut-edge innovation. The development of the brand new fourth-generation synchrotron radiation is an inevitable trend and will be of great use in revealing physical and chemical characterizations at even smaller scale (down to nano-scale). At present, diffraction-limited storage rings (DLSR) [11, 12] and X-ray free electron laser (XFEL) [13-15] make up two mainstreams of the fourth-generation light sources. Diffraction-limited storage rings (DLSR), also called "ultra-low emittance storage rings", refer to the synchrotron facilities where the emittance of the electron-beam in the storage ring is smaller or at least comparable to the emittance of the X-ray photon beam they produce at the end of their insertion devices. An already existing DLSR is MAX IV located in Lund, Sweden and other facilities such as Sirius (Campinas, Brazil) and Advanced Photon Source (Argonne, USA) are also under construction. It turns out that the brilliance of DLSR is increasing by several orders compared with the third-generation SR but they still cannot compete with XFEL, especially in the aspect of peak brightness. The extremely high peak brightness and femtosecond pulse duration of XFEL make it ideal for ultra-fast resolution and single-shot experiments, for example, German scientists [16] have already conducted crystallography experiments at the European XFEL (Germany) to reconstruct three different protein molecules by taking thousands of pictures.

1.4 *Introduction to Takagi-Taupin (T-T) equations*

After a brief review of the experimental part, we should turn our eyes upon the corresponding theoretical investigations, such as how waves propagate inside the crystal.

The Takagi-Taupin equations play a dominant role in the dynamical theory of X-ray diffraction. Before introducing the Takagi-Taupin equations, let us briefly review the history of the dynamical theory. The first dynamical theory was formulated by Darwin in 1914 [17], then Ewald extended this theory to X-rays' case in 1916 [18]; Followed by that, Laue [19, 20] solved Maxwell's equations in a periodic medium (crystal) in the form of what now is known as Bloch-waves (wavefields) in 1931. Since X-rays are essentially electromagnetic waves, their propagation in the continuous medium is to be governed by the celebrated Maxwell's equations [21]:

$$\begin{aligned} \nabla \times \mathbf{H} &= \frac{\partial \mathbf{D}}{\partial \mathrm{t}} + \mathbf{j}, \\ \nabla \times \mathbf{E} &= -\frac{\partial \mathbf{B}}{\partial \mathrm{t}}, \\ \nabla \cdot \mathbf{E} &= \rho, \\ \nabla \cdot \mathbf{B} &= 0. \end{aligned} \tag{1.9}$$

The Maxwell equations of SI units are used. In this equation set, ρ is the density of current; the electric field $\mathbf{E}$, the magnetic induction $\mathbf{B}$, the electric displacement $\mathbf{D}$ and the magnetic field $\mathbf{H}$ are related. $\mathbf{D}$ and $\mathbf{B}$ are related to the electric field $\mathbf{E}$ and the magnetic induction $\mathbf{B}$ by the material relations: $\mathbf{D} = \epsilon\mathbf{E}$ and $\mathbf{B} = \mu\mathbf{H}$ with ϵ being the dielectric constant and μ being the magnetic permeability.

The basic assumption made by Laue is the positive and negative charges are distributed continuously throughout the entire crystal. Globally, due to the neutrality of the crystal, the local electric charge and density of current equal zero, and the Maxwell's equations are reduced to:

$$\begin{aligned} \nabla \times \mathbf{H} &= \frac{\partial \mathbf{D}}{\partial \mathrm{t}}, \\ \nabla \times \mathbf{E} &= -\frac{\partial \mathbf{B}}{\partial \mathrm{t}}, \end{aligned} \tag{1.10}$$

$$\nabla \cdot \mathbf{E} = 0,$$

$$\nabla \cdot \mathbf{B} = 0.$$

The medium is polarized induced by the electric field and $\mathbf{E} = \mathbf{D}/\epsilon$, with ϵ being denoted as $\epsilon = \epsilon_0(1 + \chi)$, where χ characterizes the continuous dielectric susceptibility, or polarizability, and can be expanded in a Fourier series because it is triply periodic. By eliminating **D**, **H** and **B** in (1.10), a wave equation for the electrical field can be obtained:

$$\nabla \times (\nabla \times \mathbf{E}) - 4\pi^2 k^2 (1 + \chi)\mathbf{E} = 0 \qquad (1.11)$$

where k is the wave number, given by $k = 1/\lambda$. It is worth mentioning that in the case of hard X-rays, χ is much smaller than 1, the electric field can be approximated as:

$$\mathbf{E} = \frac{\mathbf{D}}{\epsilon_0(1+\chi)} \simeq \frac{\mathbf{D}}{\epsilon_0}(1 - \chi) \qquad (1.12)$$

Using this expression and eliminating **H** in the first two equations of Maxwell's equations (Eqn. (1.10)), one can obtain:

$$\Delta\mathbf{D} + \nabla \times \nabla \times (\chi\mathbf{D}) + 4\pi^2 k^2 \mathbf{D} = 0 \qquad (1.13)$$

This equation is simply named the "propagation equation" as it describes the propagation of an electromagnetic wave in the crystalline medium.

Combining the Fourier series of the polarizability, the wavevectors relation: $K_0 + h = K_h$ (K_0 being the refracted wavevector and K_h being the diffracted wavevector) and the Bloch's theorem: $D = \sum_h D_h \exp(-2\pi i\, \mathbf{K_h} \cdot \mathbf{r}) = 0$, we can obtain the relation for all the Fourier coefficients:

$$\sum_h [4\pi^2 (K^2 - K_h^2)\mathbf{D_h} - 4\pi^2 \sum_{h'} \chi_{h-h'} [K_h \times (K_h \times \mathbf{D_{h'}})]] = 0 \quad (1.14)$$

When all the Fourier coefficients are equal to zero, the equation satisfying all the wavevectors K_h becomes:

$$(K^2 - K_h^2)D_h - \sum_{h'} \chi_{h-h'}[K_h \times (K_h \times D_{h'})] = 0 \qquad (1.15)$$

This is the fundamental equation of the dynamical theory of X-ray diffraction.

One should be aware that the Darwin's, Ewald's and Laue's dynamical theories are only valid for plane waves and applied to perfect crystals with the crystal geometry of plane parallel slab. However, the rigorous plane wave does not exist since all the current X-ray sources are considered to produce spherical waves and real crystals may have imperfections as well. Therefore, this theory had to be developed in order to extend to the case of spherical waves. This led to birth of the well-known Takagi-Taupin equations (T-T equations), which is considered as a big milestone in the dynamical theory of X-ray diffraction.

It has been common knowledge that numerous laws, especially in the field of natural science and economics, can be formulated as differential equations that relates one or more functions and their derivatives. In general, differential equations can be classified to ordinary differentials equations, partial differential equations and nonlinear partial differential equations. In real applications, the functions represent physical quantities, and the derivatives represent their rates of change and differential equations define the relationship between them. The principle also applies to the dynamical theory of X-ray diffraction. Initially, T-T equations was formulated by Takagi [22, 23] who aimed to generalize the dynamical theory for any type of beam incident onto imperfect crystals with arbitrary deformation. In 1964, Taupin [24] independently derived equations which are quite similar to Takagi's equations, and it turns out that these two equations are equivalent except a minor difference in the choice of wavevectors. In honour of their outstanding contributions, these equations are then named as "T-T equations". The T-T equations are derived on the basis of the classical Maxwell's and are generally considered to possess a solid basis. With regard to the sample geometry, a typical geometry discussed by

Borrmann & Lehmann [25] is semi-infinite flat crystal with lateral surfaces taken into account.

In fact, T-T equations consist of two partial differential equations (PDEs) and can be expressed in the following form:

$$\frac{\partial D_0(\mathbf{r})}{\partial x_o} = -\mathrm{i}\pi k C \chi_{\bar{h}} D_h(\mathbf{r}); \tag{1.16a}$$

$$\frac{\partial D_h(\mathbf{r})}{\partial x_h} = -\mathrm{i}\pi k C \chi_h D_0(\mathbf{r}) + \mathrm{i} \cdot 2\pi k \beta_h D_h(\mathbf{r}) \tag{1.16b}$$

In this equation, $D_0(\mathbf{r})$ and $D_h(\mathbf{r})$ represent the amplitudes for the refracted and diffracted beams, $\mathbf{r}$ is the position vector in real space, x_o and x_h represent the unit vectors along the direction of the transmitted and diffracted beams, respectively. C stands for the polarization factor and equals 1 for σ polarization and cos $2\theta_B$ for π polarization with θ_B being the exact Bragg angle, χ_h and $\chi_{\bar{h}}$ are the Fourier coefficients of dielectric susceptibility, β_h is the resonance error describing the deviation from the exact Bragg condition for a specific lattice plane.

As for the solutions to this equation set, the T-T equations do not usually have analytical solutions, instead, they can be solved by using the Riemann-Green method [26]. Nevertheless, there are still two special cases where analytical solutions are obtained: one is that the incident X-ray radiation impinges onto a perfect crystal and the X-rays are produced by a spherical source; the other case is that the crystal is deformed but with a constant strain gradient.

If a sample used in an experiment is highly perfect, as a good reference, we consider the perfect crystal case. Based on this assumption, the term $\mathrm{i} \cdot 2\pi k \beta_h D_h(\mathbf{r})$ in Eqn. (1.16b) can be omitted because β_h can be put to zero after a proper choice of the wavevectors. The two equations are then transformed to Eqn. (1.17) and it is easily recognized that they possess the intrinsic hyperbolic nature.

$$\frac{\partial D_0(\mathbf{r})}{\partial x_o} = -\mathrm{i}\pi k C \chi_{\bar{h}} D_h(\mathbf{r}), \tag{1.17a}$$

$$\frac{\partial D_h(\mathbf{r})}{\partial x_h} = -\mathrm{i}\pi k C \chi_h D_0(\mathbf{r}). \tag{1.17b}$$

These equations are also consistent with both the experimental and theoretical results, *i.e.*, the characteristic lines of these two equations are completely overlapped with the refracted beam and reflected beam which constitute the so-called "Borrmann triangle" (also referred to as Borrmann fan) and this explains the formation of the Borrmann triangle in a mathematical sense [27].

The T-T equations have some practical applications where the deformation within the crystal is not negligible. In these cases, researchers usually take advantage of the computational method to solve the T-T equations and this may provide insight into X-ray optical devices, for instance, Mocella [28] resolved the Takagi-Taupin equations for X-ray optics and applies to a thermally deformed crystal monochromator with an assumption of incoherent X-ray source illumination; Honkanen [29] developed a computationally efficient method to calculate the reflectivity curve of a large deformed crystal and it turns out that the theoretical and experimental reflectivity curves show profound agreement.

1.5 *Summary*

It has been well demonstrated that synchrotron sources have many fascinating advantages. The most important advantage of synchrotron radiation over a lab X-ray source is its brilliance. In general, the brilliance of synchrotron sources is more than a billion times higher than conventional X-ray lab sources. Higher brilliance makes it possible to 'see' more detail in the sample under investigation. That is why the request for increased brilliance is so crucial. In addition, some other useful properties of synchrotron radiation are: high energy X-ray beams

may well penetrate into the sample and are suitable for digging into tiny features; synchrotron beams can be highly coherent, which is appropriate for permitting specific experiments; pulsed time structure can unlock the secret of chemical reactions on a very short time scale, *etc*. Until now, SR has been widely used for a diversity of advanced research: biology (macromolecular/protein crystallography [30]), chemistry (the operation of catalysts in large chemical engineering processes [31]), materials science (high resolution imaging [32] with the aim of nanoscale-imaging of surfaces, thin films and porous materials), environmental sciences and agriculture [33], industry (synchrotron X-ray imaging of industrial processes for industrial applications [34, 35]) and engineering (LIGA process [36]). Despite this, one still needs to focus the beam in cases of small sample, weak scattering objects and the possibility of imaging. The background for, and details of X-ray's focusing devices will be discussed in detail in Chapter 2.

In order to understand the physics of wave propagation in such devices, the diffraction theories have to be applied. We have thus also, in the last subchapter reviewed the development of the dynamical theory of X-ray diffraction and derived the fundamental equations of the dynamical theory. Followed by that, the T-T equations are discussed in detail because they extend the previously formulated theory to more general cases.

1.6 *References*

[1] Authier, A., 2012. The Early Days of X-ray Diffraction.
[2] Iwanenko, D. and Pomeranchuk, I., 1944. On the maximal energy attainable in a betatron. Physical Review, 65(11-12), p.343.
[3] Blewett, J.P., 1946. Radiation losses in the induction electron accelerator. Physical Review, 69(3-4), p.87.
[4] Blewett, J.P., 1988. Synchrotron radiation—1873 to 1947. Nuclear Instruments and Methods in Physics Research Section A: Accelerators, Spectrometers, Detectors and Associated Equipment, 266(1-3), pp.1-9.

[5] Schwinger, J., 1949. On the classical radiation of accelerated electrons. Physical review, 75(12), p.1912.
[6] Tomboulian, D.H. and Hartman, P.L., 1956. Spectral and angular distribution of ultraviolet radiation from the 300-Mev Cornell synchrotron. Physical Review, 102(6), p.1423.
[7] del Rio, M.S. and Dejus, R.J., 2004, October. Status of XOP: an x-ray optics software toolkit. In Advances in Computational Methods for X-Ray and Neutron Optics (Vol. 5536, pp. 171-174). International Society for Optics and Photonics.
[8] Sasaki, S., Kakuno, K., Takada, T., Shimada, T., Yanagida, K.I. and Miyahara, Y., 1993. Design of a new type of planar undulator for generating variably polarized radiation. Nuclear Instruments and Methods in Physics Research Section A: Accelerators, Spectrometers, Detectors and Associated Equipment, 331(1-3), pp.763-767.
[9] Kimura, S.I., Kamada, M., Hama, H., Marechal, X.M., Tanaka, T. and Kitamura, H., 1996. Design of a helical undulator for UVSOR. Journal of electron spectroscopy and related phenomena, 80, pp.437-440.
[10] Snigirev, A., Snigireva, I., Kohn, V., Kuznetsov, S. and Schelokov, I., 1995. On the possibilities of x-ray phase contrast microimaging by coherent high-energy synchrotron radiation. Review of scientific instruments, 66(12), pp.5486-5492.
[11] Eriksson, M., van der Veen, J.F. and Quitmann, C., 2014. Diffraction-limited storage rings–a window to the science of tomorrow. Journal of synchrotron radiation, 21(5), pp.837-842.
[12] Al-Dmour, E., Ahlback, J., Einfeld, D., Fernandes Tavares, P.F. and Grabski, M., 2014. Diffraction-limited storage-ring vacuum technology. Journal of synchrotron radiation, 21(5), pp.878-883.
[13] Huang, Z. and Kim, K.J., 2007. Review of x-ray free-electron laser theory. Physical Review Special Topics-Accelerators and Beams, 10(3), p.034801.
[14] McNeil, B.W. and Thompson, N.R., 2010. X-ray free-electron lasers. Nature photonics, 4(12), p.814.

[15] Ishikawa, T., Aoyagi, H., Asaka, T., Asano, Y., Azumi, N., Bizen, T., Ego, H., Fukami, K., Fukui, T., Furukawa, Y. and Goto, S., 2012. A compact X-ray free-electron laser emitting in the sub-ångström region. nature photonics, 6(8), pp.540-544.
[16] Grünbein, M.L., Bielecki, J., Gorel, A., Stricker, M., Bean, R., Cammarata, M., Dörner, K., Fröhlich, L., Hartmann, E., Hauf, S. and Hilpert, M., 2018. Megahertz data collection from protein microcrystals at an X-ray free-electron laser. Nature communications, 9(1), pp.1-9.
[17] Darwin, C.G., 1914. XXXIV. The theory of X-ray reflexion. The London, Edinburgh, and Dublin Philosophical Magazine and Journal of Science, 27(158), pp.315-333.
[18] Ewald, P.P., 1916. Zur begründung der kristalloptik. Annalen der Physik, 354(1), pp.1-38.
[19] von Laue, M., 1931. Die dynamische Theorie der Röntgenstrahlinterferenzen in neuer Form. In Ergebnisse der exakten naturwissenschaften (pp. 133-158). Springer, Berlin, Heidelberg.
[20] von Laue, M., 1931. Ergebnisse der exakten naturwissenschaften. Naturwissenschaften, 10, pp.207-284.
[21] Jackson, J.D., 1999. Classical electrodynamics, 3rd edn. John Wiley and Sons, New York.
[22] Takagi, S., 1962. X-ray dynamical diffraction theory for ideal crystals. Acta cryst, 15, pp.1131-1138.
[23] Takagi, S., 1969. A dynamical theory of diffraction for a distorted crystal. Journal of the Physical Society of Japan, 26(5), pp.1239-1253.
[24] Taupin, D., 1964. Dynamic theory of x-ray diffraction in crystals. Bull Soc Fr Mineral Crystallogr, 87.
[25] Borrmann, G., and Lehmann K., 1963. Crystallography and Crystal Perfection, edited by GN RAMACHANDRAN, Vol. A, pp.101-108.
[26] Thorkildsen, G. and Larsen, H.B., 1999. X-ray intensity patterns from finite perfect crystals. Acta Crystallographica Section A: Foundations of Crystallography, 55(6), pp.1000-1013.

[27] SUN, Z.D. and LIANG, J.G., A NEW METHOD OF SOLVING THE TAKAGI EQUATION OF THE DYNAMICAL THEORY OF X-RAY DIFFRACTION.
[28] Mocella, V., Lee, W.K., Tajiri, G., Mills, D., Ferrero, C. and Epelboin, Y., 2003. A new approach to the solution of the Takagi–Taupin equations for X-ray optics: application to a thermally deformed crystal monochromator. Journal of applied crystallography, 36(1), pp.129-136.
[29] Honkanen, A.P., Monaco, G. and Huotari, S., 2016. A computationally efficient method to solve the Takagi–Taupin equations for a large deformed crystal. Journal of Applied Crystallography, 49(4), pp.1284-1289.
[30] Maleknia, S.D., Ralston, C.Y., Brenowitz, M.D., Downard, K.M. and Chance, M.R., 2001. Determination of macromolecular folding and structure by synchrotron x-ray radiolysis techniques. Analytical biochemistry, 289(2), pp.103-115.
[31] Thomas, J.M. and Sankar, G., 2001. The Role of Synchrotron-Based Studies in the Elucidation and Design of Active Sites in Titanium− Silica Epoxidation Catalysts. Accounts of Chemical Research, 34(7), pp.571-581.
[32] Nasse, M.J., Walsh, M.J., Mattson, E.C., Reininger, R., Kajdacsy-Balla, A., Macias, V., Bhargava, R. and Hirschmugl, C.J., 2011. High-resolution Fourier-transform infrared chemical imaging with multiple synchrotron beams. Nature methods, 8(5), pp.413-416.
[33] Hernandez-Viezcas, J.A., Castillo-Michel, H., Andrews, J.C., Cotte, M., Rico, C., Peralta-Videa, J.R., Ge, Y., Priester, J.H., Holden, P.A. and Gardea-Torresdey, J.L., 2013. In situ synchrotron X-ray fluorescence mapping and speciation of CeO2 and ZnO nanoparticles in soil cultivated soybean (Glycine max). ACS nano, 7(2), pp.1415-1423.
[34] Schenk, T.A., Thi, H.N., Gastaldi, J., Reinhart, G., Cristiglio, V., Mangelinck-Noël, N., Klein, H., Härtwig, J., Grushko, B., Billia, B. and Baruchel, J., 2005. Application of synchrotron X-ray imaging to the

study of directional solidification of aluminium-based alloys. Journal of Crystal Growth, 275(1-2), pp.201-208.
[35] Baruchel, J. and Kvick, Å., 2004. Synchrotron radiation imaging and diffraction for industrial applications. europhysics news, 35(2), pp.50-55.
[36] Becker, E., Ehrfeld, W., Hagmann, P., Maner, A. and Münchmeyer, D., 1986. Fabrication of microstructures with high aspect ratios and great structural heights by synchrotron radiation lithography, galvanoforming, and plastic moulding (LIGA process). Microelectronic engineering, 4(1), pp.35-56.

2 X-ray beam conditioning devices

As has been reviewed in Chapter 1, the newly built SR sources are capable of producing high-quality X-ray beam with lots of desired properties, such as high brilliance, low emittance and good coherence. There was once a heated argument "no optics is the best optics", it was in principle true but the required experimental conditions (a non-modified "pink beam" which has the bandwidth on the order of $\Delta E/E \backsimeq 5 \times 10^{-2}$ and all should be in vacuum to avoid any contamination) are too harsh to be satisfied for the time being.

Based on this, X-ray optical devices are still needed in order to deliver an even more optimized X-ray beam for experiments, which directly leads to the revival of X-ray optics - a branch of optics that aims to manipulate X-rays in analogy to visible light, or more specifically, the beam impinging on the sample should be properly conditioned to achieve maximum intensity, well-defined spectral and angular widths, a very wide but still tunable energy range, *etc*.

In general, conditioning of the beam is optimized for experimental setups, which is usually fulfilled by a combination of monochromators and focusing devices. Monochromators will select a specific single wavelength (or energy) beam by tuning automatically, and focusing devices will provide a focused beam with higher intensity for the investigation of very small samples and trace elements in the materials. Both of these two types will be introduced in this chapter.

2.1 *Monochromators*

As a matter of fact, a majority of experimental arrangements at a SR source require a monochromatic beam. However, SR sources produce polychromatic X-ray radiation and this leads to the proposal of so-called "monochromator" [1] (Fig. 10).

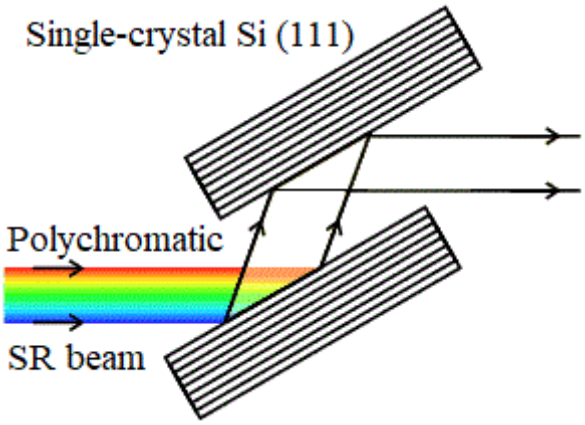

Figure 10 – A schematic drawing of a typical monochromator in the so-called $(+,-)$ setting. The notation $(+,-)$ means that the incident beam on the first crystal and the reflected beam from the second crystal are on the different side of the crystals and is depicted in the figure above; in comparison, the $(+,+)$ monochromator arrangement represents that the incident and reflected beams come from the same sides of the crystals. Besides, one should note that the widely used nomenclatures $(+n,+n)$ and $(+n,-n)$ represent the reflections come from identical reflections of the same order lattice planes (nth order).

The word "monochromator" originally comes from Greek, which literally means a device capable of separating light having different colours into one. In the early days, monochromatization of the incident beam could only be done by choosing appropriate absorbing filters; later on, it was realized that a better way was taking advantage of Bragg reflection of the incident beam on a crystal since the atoms in the crystal are arranged periodically in three-dimensional space and each of them is considered as a scatterer. Under the excitation of the incoming X-ray beam, these independent scatterers are then forced to vibrate and emit scattered waves that have the same wavelength as the source but differ in directions. In other words, it is elastic scattering essentially. As a result, destructive interference may occur in most directions; however, in some specific directions, constructive interference may be produced because of phase interference. Based on this mechanism, the crystal monochromator is able to select radiation of a single wavelength or energy from a wider range of wavelengths.

Since most monochromators work in Bragg geometry, Bragg's law will be briefly reviewed here. In 1913, Bragg diffraction was proposed by Lawrence Bragg and his father William Henry Bragg [2] in order to interpret Laue's diffraction pattern that crystalline solids produce sharp peaks of reflected X-rays at some specific wavelengths and incident angles. In essence, Bragg's law is equivalent to the interference equation and is a special case of Laue diffraction. In fact, Bragg's law transforms the problem from the reciprocal space to the direct space and accounts for the result of X-ray interference without involving the physical process of diffraction. Bragg's law can be directly derived from the concept of crystal reflection, as is shown in Fig. 11. When the scattered waves interfere constructively, they remain in phase since the optical path of the two waves ($PO'Q$) between the adjacent lattice planes is equal to an integer multiple of the wavelength (Fig. 11), expressed as:

$$2d_{hkl}\sin\theta_B = \lambda \tag{2.1}$$

where d is interplanar distance of the lattice planes and its subscripts hkl represent the corresponding Miller indices of the lattice planes, θ_B is the angle between the incident beam and the planes, λ is the wavelength of the incident radiation.

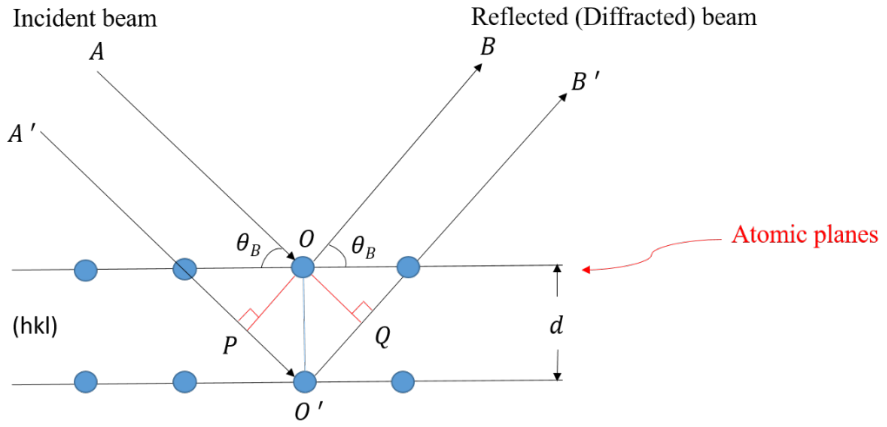

Figure 11 – A schematic diagram of Bragg's law.

One should pay attention to the fact that the refraction effect indeed occurs when the radiation is incident onto the entrance surface (vacuum-to-crystal), however, when the reflected (diffracted) beam exits from the same interface (crystal-to-vacuum), the refraction effect takes place again and these two cancel out each other. In consequence, we can neglect the refraction effect in this case. In addition, it is worth mentioning that Bragg's law is also applied to the cases of neutron and electron diffraction. In spite of its simple form, Bragg's law plays a vital role in determining the structure of crystals by analysing the diffraction patterns recorded on films or detectors.

When evaluating the performance of monochromators, it is necessary to study its bandwidth and this is usually done by differentiation the Bragg's law in Eqn. (2.1):

$$\Delta\lambda = 2d_{hkl}\cos\theta_B \cdot \Delta\theta \tag{2.2}$$

where $\Delta\lambda$ characterizes the range of the reflected wavelength, $\Delta\theta$ characterizes the angular divergence of the beam diffracted by the crystal and other parameters have their usual meanings.
The bandwidth is then denoted as:

$$\frac{\Delta\lambda}{\lambda} = \frac{\Delta E}{E} = \frac{\cos\theta_B \cdot \Delta\theta}{\sin\theta_B} = \cot\theta_B \cdot \Delta\theta \tag{2.3}$$

The divergence of the beam diffracted by the crystal depends on both the 'full width at half maximum' (FWHM) or Darwin width ($2\delta_{os}$) of the rocking curve and the natural divergence of the incident beam, Ω. The so-called "rocking curve" [3, 4] (a plot of experimental data which depicts the relationship between X-ray intensity VS rocking angles and the rotational direction is along ω-axis shown in Chapter 3) is usually used to reveal broadening of diffraction peaks caused by imperfections of the crystal, such as mosaicity, strain, *etc*.). Here one should distinguish the experimentally obtained rocking curve from the theoretical reflectivity curve, in fact, the former can be seen as a convolution of the

theoretical reflectivity curve, apparatus function and broadening due to various kinds of defects [5].

The energy resolution can then be expressed as a quadratic sum of these two terms: $\Delta\theta = \sqrt{\Omega^2 + (2\delta_{os})^2}$. In general, the monochromator works in the $(+n, -n)$ non-dispersive setting (Fig. 12), which means the reflecting planes of the two crystals are parallel. More specifically, if ray 1 (black) satisfies Bragg's condition on the crystal and ray 2 (red) for another wavelength, both of them will satisfy Bragg's condition on the second crystal, the setting is said to be non-dispersive.

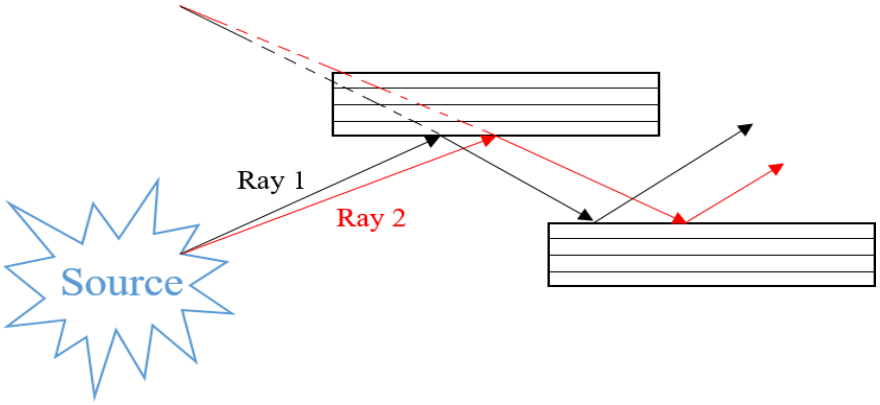

Figure 12 – Experimental arrangement of a monochromator in $(+n, -n)$ non-dispersive setting.

It is to be noted that in this special case, the energy resolution of the monochromator is solely dependent on the width of the rocking curve. Based on the dynamical theory of X-rays, the FWHM of highly perfect crystals is smaller than that of imperfect crystals and that is why a monochromator is often fabricated out of perfect crystals, such as germanium (Ge), silicon (Si) and even locally dislocation free diamond (C). Most monochromators work in the reflection or Bragg geometry and the key parameter - Darwin width $(2\delta_{os})$ [6] is used and given by:

$$2\delta_{os} = \frac{2R\lambda^2}{\pi V \sin 2\theta_B}\sqrt{|\gamma|}|C|\sqrt{F_h F_{\bar{h}}} \qquad (2.4)$$

In this equation, R is the classical radius of the electron and reflects the

strength of the interaction process, λ is the wavelength of incoming beam, V is the volume of the unit cell, γ is the asymmetry ratio, C is the polarization factor, the structure factor F_h is used to describe the amplitude and phase of a wave diffracted from lattice planes of Miller indices h, k, l while $F_{\bar{h}}$ corresponds to those with negative h, k, l.
By substituting Eqn. (2,1) and (2.4) into (2.3), and using the "double-angle" identity of $\sin(2\theta_B) = 2\sin(\theta_B)\cos(\theta_B)$, the bandwidth of the monochromator can be written as:

$$\frac{\Delta\lambda}{\lambda} = \frac{\cos\theta_B}{\sin\theta_B} \cdot \frac{2R(2d_{hkl}\sin\theta_B)^2}{\pi V 2\sin\theta_B\cos\theta_B}\sqrt{|\gamma|}|\mathrm{C}|\sqrt{F_h F_{\bar{h}}}$$
$$= \frac{4Rd_{hkl}{}^2}{\pi V}\sqrt{|\gamma|}|\mathrm{C}|\sqrt{F_h F_{\bar{h}}} \quad (2.5)$$

It has been textbook knowledge that the lattice spacing d_{hkl} for higher order reflections is smaller and the corresponding Bragg angle θ_B is larger. In other words, high order reflections have narrower bandwidths compared with lower order reflections, but this is at the cost of loss of intensity.

As for the selection of monochromator crystal, two parameters should be taken into consideration carefully when evaluating its performance: one is the energy resolution (or bandwidth) and the other is the resistance to the strong heat load. Now let us move on to the second one. When a monochromator is heated, thermal gradients are to set up across the crystal and then may cause distortions, which severely deteriorate its optical performance. Therefore, these undesired effects should be minimized by taking advantage of cooling methods. By now, two methods have been commonly used, they are water-cooling and cryogenic cooling, respectively. Either can be chosen in real experiment depending on the heat load needs to be dissipated and other specific experimental requirements. In comparison, Cryogenic cooling is considered more efficient than water-cooling because for the most common monochromator material-silicon, the ratio of the thermal conductivity coefficient k to the thermal expansion coefficient α (characterized by k/α) is far smaller at liquid nitrogen temperature than

room temperature. Likewise, the crystals with high k/α are suitable for manufacturing monochromators because they are still very stable even though bathed in strong synchrotron radiation. In general, monochromators can be divided into two types: channel-cut monochromators (CCM) and double-crystal monochromators (DCM).

2.1.1 Channel-cut monochromator

A channel-cut monochromator can be used for experiments with hard X-rays and it simply employs a crystal to be slotted in the middle and the beam is then diffracted by two opposite sides of the groove. Since the two diffractive crystals are from a single piece of crystal, they are integrated and this ensures good parallelism between the planes. CCM do not have the drawback of being instable that DCM have and can achieve fast tuning, high transmission efficiency and a narrow energy band. However, the main disadvantage is the exit beam deviate from the direction of the incident beam and this results in the proposal of so-called "four-crystal monochromator" [7] to get a fix-exit beam.

It employs a crystal to be slotted in the middle and the beam is diffracted by two opposite sides of the groove. Since the two diffractive crystals are integrated, this type of monochromator can achieve fast tuning, meanwhile, the transmission efficiency is high, the energy band is narrow, and the structure is relatively simple. Nevertheless, when selecting or scanning the wavelength, the position of the output beam changes as the incident angle changes.

2.1.2 Double crystal monochromators

The double-crystal monochromator is suitable for use for all the current SR sources. Literally, the double crystal monochromator consists of two separate crystals in $(+,-)$ configuration (Fig. 10) that are arranged in parallel to produce a monochromatic exit beam which is running parallel

to the incident white X-ray beam. By means of coaxial rotation, the alignment is adjusted to perform dynamic scanning.

In fact, these two types are kind of similar and CCM can be seen as a simple construction of DCM and both of them are used in the experimental setups introduced in Chapter 3.

2.2 *X-ray focusing devices*

A lot of useful X-ray techniques such as X-ray crystallography, small-angle X-ray scattering, wide-angle X-ray scattering, X-ray fluorescence, X-ray spectroscopy and X-ray photoelectron spectroscopy *etc*., require high X-ray flux densities shining onto the sample under investigation and this is usually achieved by using a focusing optical element to focus the divergent beam from the X-ray source. What's more, it turns out that focused X-ray beam is also preferred for scanning probe techniques such as scanning transmission X-ray microscopy and scanning X-ray fluorescence imaging. All these techniques benefit a lot from focused X-ray beam with high flux densities, which in turn, drives the development of X-ray focusing devices. Looking back upon the history, no one had been able to figure out an efficient way to focus X-rays even 50 years after their discovery because they interact with matter so weakly that they are almost unable to focus. As a matter of fact, the pioneer of X-ray focusing optics was the discoverer - Röntgen himself, who had tried to focus X-rays with a prism but unfortunately, he failed in the end. Due to the recent progress of material science and high-precision microfabrication technology, it has become possible to manufacture high-efficiency X-ray focusing components, such as X-ray mirrors (K-B mirrors), Fresnel zone plates (FZPs) and compound refractive lenses (CRLs). These will be reviewed in the following section.

2.2.1 X-ray mirrors (K-B mirrors)

X-ray mirrors, are also usually referred to as “K-B mirrors” in honour of Kirkpatrick and Baez (also known as “fathers” of X-ray microscope) [8] who designed the prototype. It is worth mentioning that this big invention marks the real beginning of X-ray optics.

In the light of geometrical optical theory, reflecting light with a single curved mirror may produce a severe astigmatism, focusing rays from a point source to a line. Since a line focus is always more desired, Kirkpatrick wisely proposed to place a second curved mirror at a right angle to squeeze the line focus from the first mirror down to a point. In consequence, a K-B mirror system typically consists of a pair of metal bars placed at right angles to each other (each with one side polished to a brilliant shine). In general, two geometric shapes are chosen for the curved surfaces: a parabolic mirror shape [9] will focus a well collimated beam to a point, while an elliptical mirror shape [10] will focus a point to another point. Fig. 13 is a sketch of K-B mirrors which are under the vertical configuration.

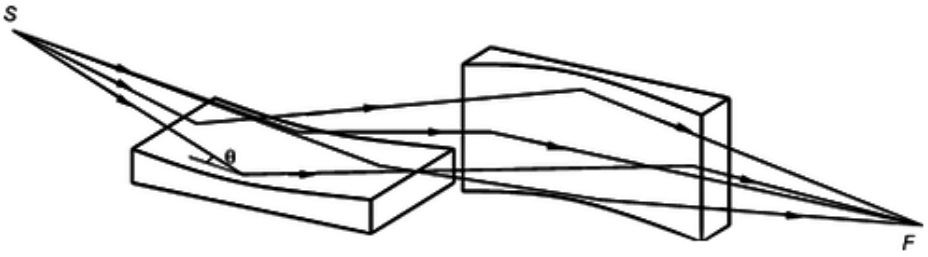

Figure 13 – X-ray mirror setting; S: the source; θ: the glancing angle; F: the focusing spot.

Since K-B mirrors work by reflecting X-rays off a curved surface, one side of each mirror (metal bar) should be polished to a very brilliant shine to ensure sufficient mirror reflection and the surface roughness is thus a key criterion to evaluate their performance. As the grazing incidence angle lies in the order of several milliradians, even tiny flaw in optical precision will lead to unacceptable consequences. For this reason, low−

level polishing and metal-coating techniques in 1940s largely postponed the mirrors' fast application. It was not until 1970s when the scientists were able to make ultra-smooth surfaces; nowadays, the modern and advanced fabrication technology [11] is capable of polishing the material exquisitely, enabling to decrease the surface roughness down to nanometer scale (the roughness of the world's best K-B mirrors has been decreased to sub-nanometer scale [12, 13]); otherwise, the rough surface may scatter the photons out of the focus, which significantly deteriorate the focusing effect. To pursue better performance in experiments, larger apertures are ideal and so is the critical angle. The maximum aperture of the mirrors does not exceed the value of the critical angle ω_c and its expression is given by Authier [6]:

$$\omega_c = \lambda\sqrt{\frac{RF_0}{\pi V}} \tag{2.6}$$

where F_0 is the structure factor and the other symbols have their usual meanings (refer to Eqn. (2.4)). From Eqn. (2.6), it can be easily inferred that the critical angle increases with the atomic number, and the material with a heavier element is thus more suitable. Regarding the potential materials, the first K-B mirrors were made of glass or quartz coated with a reflective metal film, but today's mirrors are typically made from silicon crystals polished to near-atomic smoothness and then coated with a very thin layer of gold or platinum down to atomic-level precision. In addition to functioning as an efficient focusing device for various experimental setups, K-B mirrors can also be implemented as an energy filter to select X-rays below a certain cut-off energy, for instance, they can remove higher-order harmonics arising from Bragg reflections from the monochromators.

To conclude, compared with other focusing elements, the main advantage of K-B mirrors is that they are able to reflect X-rays with different energies uniformly and they have been installed for advanced coherent X-ray imaging systems. The disadvantage is also quite obvious: K-B mirrors are so sensitive that even a tiny roughness on the surface or

temperature fluctuations may deviate the beam from the focus. Besides, K-B mirrors are off-axis focusing elements from their operating principle and the calibration process is deemed to be both time-consuming and complicated.

2.2.2 Fresnel zone plates (FZPs)

A Fresnel zone plate [14] (Fig. 14) is constituted by a set of radially symmetric rings, which alternate between opaque and transparent. The zones can be spaced such that the optical path difference between the source and the focal point varies by $\lambda/2$ from one zone to the next. ***S*** represents the source, ***F*** the focal point and p_n is a point on the nth zone. In other words, the difference between the optical paths should be integral multiples of $\lambda/2$, denoted as:

$$\sqrt{d^2 + {r_n}^2} + \sqrt{f^2 + {r_n}^2} - (d + f) = \mathrm{n}\lambda/2 \qquad (2.7)$$

where r_n is the radius of the nth zone and n is an integer.

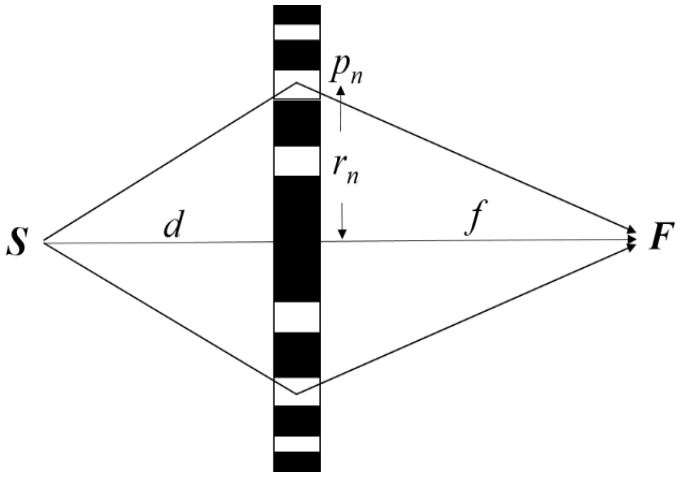

Figure 14 – Fresnel zone plates.

It is obvious that the Fresnel zone plates operate in the transmission mode, then Aristov *et al.* [15] proposed a new type called “Bragg-Fresnel

lenses" by combining the principle of Fresnel zone plates and Bragg diffraction, which means they work in the reflection geometry. The prominent advantage of the Bragg-Fresnel lenses is the beam coherence is preserved and thus they have been applied in many experiments requiring high coherence, like micro-diffraction and small-angle scattering.

2.2.3 Compound refractive lenses (CRLs)

It has been discussed that X-rays possess wave-particle duality, which practically means they may behave like light and some phenomena like refraction and reflection will also take place. As we know, refraction is a common physical phenomenon that describes the bending of light when it enters a different medium from one to another and is always described by the celebrated Snell's law: $n_1 \sin\theta_1 = n_2 \sin\theta_2$, where light enters medium 2 from medium 1 and the refractive index of medium 1 and medium 2 are n_1 and n_2, respectively. θ_1 is the angle of incidence, θ_2 is the angle of refraction. The physical interpretation for this phenomenon is: light is an electromagnetic wave with a high frequency and there are two components perpendicular to the direction of propagation, the electric field component $\boldsymbol{E}$ and the magnetic field component $\boldsymbol{H}$. When the electric field component $\boldsymbol{E}$ interacts with each atom during the propagation, electrons in the atoms will be polarized, causing the electron clouds and the nucleus to be relatively displaced. As a result, part of the energy is absorbed, in the meantime, the speed of light slows down and the propagation direction changes, resulting in the occurrence of the well-known refraction phenomenon. It is the fundamental law that forms the basis of traditional lenses aiming for modifying visible light and the refractive indexes of most materials for visible light usually lie in the range from 1.2 to 2 and vary with the frequency of light.

However, for X-rays, it is a totally different case [16]. The refraction index for electromagnetic waves displays resonant behavior at frequencies corresponding to electronic transitions in atoms and

molecules. On the low frequency side of a resonance, n increases with the frequency and this is known as normal dispersion. Once the frequency reaches to the resonance frequency, more and more resonances will pass through, causing the magnitude of the refraction index to decrease. In general, the frequencies of X-rays are higher than all transition frequencies. In other words, the refractive index n for X-rays turns out to slightly smaller than unity and is always denoted as:

$$n = \sqrt{1+\chi_0} \approx 1 + \frac{1}{2}\chi_0 \; = 1 + \frac{1}{2}\mathrm{Re}[\chi_0] + \mathrm{i}\,\frac{1}{2}\mathrm{Im}\,[\chi_0]$$
$$= 1 - \delta - \mathrm{i}\,\beta \qquad (2.8)$$

with $\chi_0 = -\frac{r_e\lambda^2}{\pi V_c}F_0$ and $F_0 = N(Z + f' + f'')$, N is the number of atoms in the unit cell with V_c being its volume, Z is the atomic number of the element, f' and f'' are the so-called anomalous dispersion factors. In the above expression, δ represents the refractive decrement and β characterizes the absorption coefficient.

At first glance, one might wonder that the conclusion seems unreasonable because the speed of light in the medium (c/n) is faster than that in vacuum with the refractive index n being smaller than 1. In reality, it should be pointed out that c/n is the phase velocity, not the group velocity characterized by $d\omega/dk$.

As the index of refraction of matter for X-rays is very close to unity, it is in principle impossible to fabricate a refractive lens in the usual way. Due to the very tiny refractive decrement (δ is usually in the order of 10^{-6}), the focusing effect of one single lens is extremely weak and the focal length is hard to fulfill in real experiments. It was not until in 1996 that Snigirev *et al.* [17, 18] proposed the prototype simply by drilling up to 31 cylindrical holes in a row out of an aluminum bulk to accumulate the refractive effect and achieve optimal focusing effect, which is schematically drawn in Fig. 15. In the meantime, Tomie [19] had almost

the same idea on focusing X-rays by means of the refraction effect. It is worth noting that CRLs are able to focus and collimate neutron sources, which have been used at neutron-related experiments [20, 21].

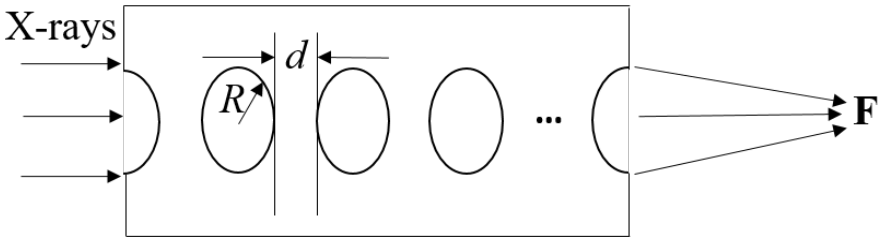

Figure 15 – The prototype of compound refractive lenses (CRLs).

It can be seen from Fig. 15 that every hole corresponds to a biconcave lens and the width of one lens d is strictly limited to several tens of microns in order to minimize the absorption effectively. Based on thin-lens approximation, the focal length for a lens can be denoted as:

$$f = \frac{R}{2\delta} = \frac{R}{2(1-n)} \tag{2.9}$$

where R represents the radius of the hole and $\delta = 1 - n$ characterizes the refractive decrement of the material. In order to achieve an optimal better focusing effect, many lenses should be stacked together on the optical path of the X-ray beam and the focal length is easily deduced to be:

$$f = \frac{R}{2(1-n)} = \frac{R}{2N\delta} \tag{2.10}$$

Here N stands for the number of holes the block and each hole actually corresponds to a biconcave lens.

In practical applications, the spherical lenses turn out to induce unwanted spherical aberrations and researchers mainly adopt the parabolic shape CRLs now.

Two different focusing effects can be achieved: a line focus and a point focus, respectively. A line focus is obtained by employing planar lenses while a point focus is readily obtained by placing the lenses in crossed geometry [22].

As for the selection of potential materials, no ideal material is suitable for all cases and should be appropriately chosen depending on different scenarios. Since CRLs function as a type of transmission devices, the absorption has to be taken into consideration. The absorption is proportional to the atomic numbers and those elements with low atomic numbers are thus preferred. In addition to aluminum, potential materials include beryllium, nickel, poly (methyl methacrylate) (PMMA) and diamond, *etc*. Beryllium CRLs [23] undergo the lowest absorption, but the material is toxic and may also distort the radiation wavefront owing to the appearance of grain boundaries introduced by the production technique mainly bared on sintering; Nickel [24] is especially suitable for focusing high energy X-rays, but one main obstacle preventing its wide use lies in its low transmission efficiency because of larger atomic numbers; in case of PMMA [25] - a transparent thermoplastic often used as an alternative to glass, the biggest obstacle to overcome is its instability after being long being exposed to strong radiation because numerous bubbles may be generated in the material because of strong heat load.

The extreme properties of diamond CRLs [26-28] outperform other candidate materials and it turns out they show great potentials because diamond possesses many exceptional physical characteristics. In a diamond, carbon atoms have a tetrahedral arrangement and each of them is connected to four other carbon atoms with a C-C-C bond angle of 109.5° (*cf.* Fig. 16(a)). The crystalline structure of diamond is of cubic symmetry (*cf*. Fig. 16(b)). Although there are 18 atoms in the figure, each corner atom is shared by eight unit cells and each atom in the center of a face is shared by two, so there are eight atoms in total per unit cell. It is

a strong, rigid three-dimensional structure of diamond that results in an infinite network of atoms (*cf.* Fig. 16(c)).

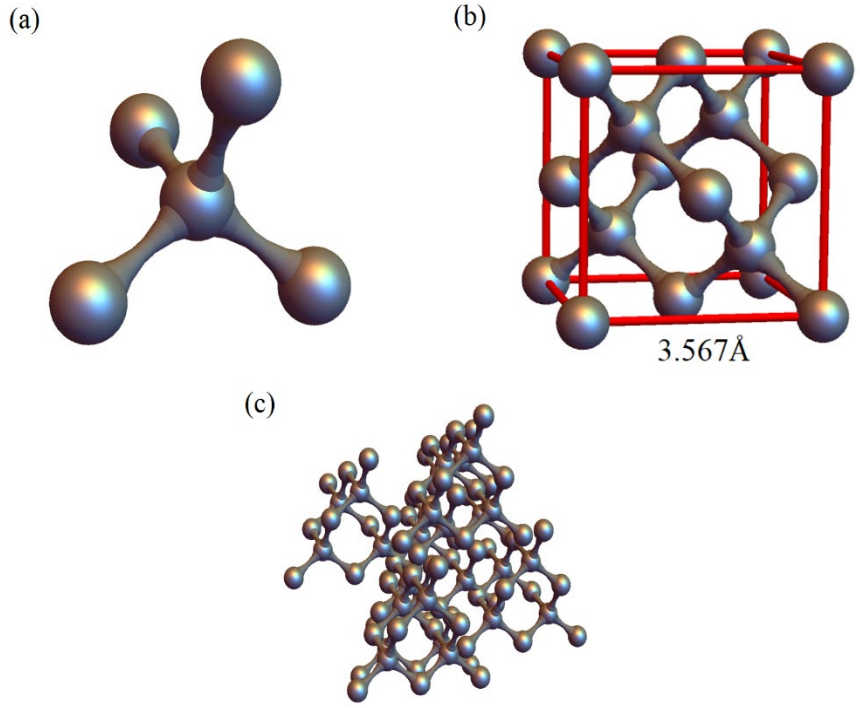

Figure 16 – (a) is the tetrahedral arrangement of carbon atoms, (b) is the unit cell of diamond at room temperature and (c) is its crystal packing [29].

Owing to this, diamond is incompressible and shows extreme hardness, which explains why researchers prefer to use diamond anvil cells (DAC) [30] to produce high pressure for scientific experiments. Besides, diamond has high thermal conductivity and very low thermal expansion, which means it can withstand strong heat load. Taking all these factors into account, diamond has become an indispensable material for some experimental techniques using synchrotron radiation as the source. Considering the extremely high cost and very limited availability of natural diamond, it is a necessity to fabricate synthetic diamonds to meet the growing demands. Synthetic diamonds can be grown from high-

purity carbon under high pressures and temperatures or from hydrocarbon gas by chemical vapor deposition (CVD). Nowadays, most industrial and scientific applications use CVD diamond and in the experimental setting at ESRF, a synthetic CVD diamond by the "Element Six" company was utilized to fabricate CRLs and the CRLs were tested at one of the beamlines at ESRF. The publications [31, 32] presented in Chapter 5 in this thesis will give more details about that.

In addition to these unique properties, diamond has a low atomic number of 6 in the periodic table, which means the absorption coefficient is relatively low. Indeed, the extreme hardness may prohibit us from polishing to an ideal shape, but thanks to the advent of femtosecond laser micromachining process [33], it has become a reality to fabricate diamond lenses with high precision. Single-crystal diamond is considered advantageous over polycrystalline diamond because it will not cause any undesired diffuse scattering induced by crystalline boundaries and avoid the drawbacks when etching a polycrystalline diamond. This explains why single-crystal diamond CRLs is preferred in the real experiment. Fig. 17 is a plot of refractive decrement and absorption coefficient versus photon energy for the material of diamond.

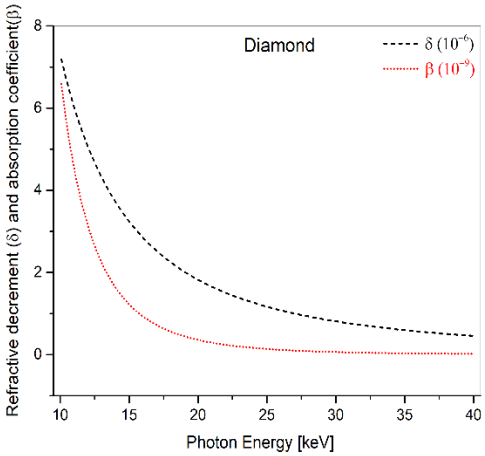

Figure 17 – The refractive decrement and absorption coefficient of diamond versus photon energy.

Based on the idea of CRLs, a more advanced version - the transfocator [34] (Fig. 18) has been proposed and then become an integral part of beamlines at modern synchrotron sources. It is comprised of several cartridges containing different numbers of lenses, such that the focal distance can be continuously adjusted by insertion or retraction of one or more of the lens cartridges in order to be compatible with the photon energy and achieve a variable focal length. It can be inferred from the context that the main advantage of transfocator lies in flexibility. In addition, this type of transfocator can be used together with monochromators and other X-ray focusing elements, leading to a significant increase in photon flux. In fact, the chromatic nature of the focusing means that the transfocator does not only naturally suppress harmonics, but it can also function as a broad-band pass monochromator which delivers extremely high flux.

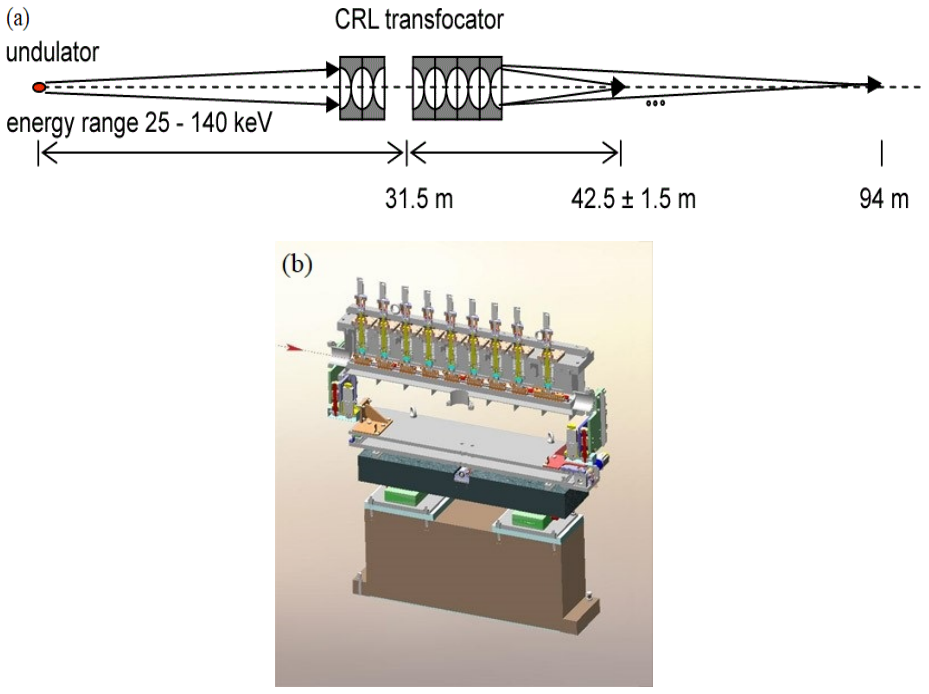

Figure 18 – (a) An example of implantation of the in-vacuum transfocator (IVT) from ESRF and (b) the design and mounting of the in-vacuum transfocator (www.esrf.eu).

In addition to the large transfocator mentioned above, a new type of "mini-transfocator" [35] with small dimensions and weight has been recently fabricated. For this reason, it is optimal for experimental techniques requiring compact and lightweight zoom-optics. What's more, it can create a customizable software for some specific experimental setups and possibly adjust to fit any control systems.

Focused X-rays can achieve high resolution in experiments and an even smaller focal spot is thus desired. In general, this is implemented by two methods: increasing the number of refractive units or decreasing the radius curvature, however, both may result in low transmission efficiency. To resolve this contradiction, the so-called "cascaded CRLs" [36] depicted in Fig. 19 has been proposed. The innovation behind the design lies in that it takes two factors into account simultaneously: large geometrical aperture and small radius curvature.

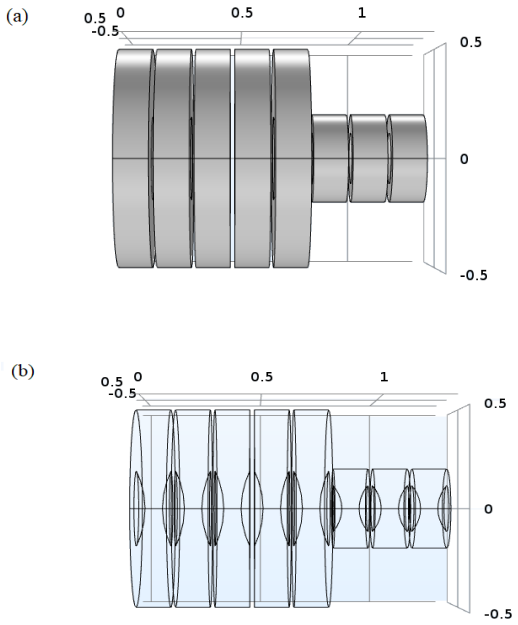

Figure 19 – (a) shows the layout of cascaded CRLs and (b) is their wireframe model. The unit is in mm.

In this conjunction, we propose to introduce a type of composite CRLs on the basis of the former cascaded CRLs. The difference between them is the former one is made of the same material while the latter one has two different materials. By applying thin-lens approximation here, the focal length f of the composite CRLs system can be written as:

$$\frac{1}{f} = \frac{1}{f_1} + \frac{1}{f_2} \tag{2.11}$$

with $f_1 = \frac{R_1}{2N_1\delta_1}$ and $f_2 = \frac{R_2}{2N_2\delta_2}$. In this equation, R_1, N_1, δ_1 are the curvature radius, number of lenses and refractive decrement for the first set of lenses; R_2, N_2, δ_2 are the same parameters for the second set.

Then the focal length of composite CRLs can be simplified to:

$$f = \frac{R_1R_2}{2R_1N_2\delta_2+2R_2N_1\delta_1} \tag{2.12}$$

To sum up, CRLs and CRL-based innovative versions have played a significant role in many scientific experiments, like being used for the rejection of higher order harmonics [37], high-resolution imaging [38] and microscopy [39].

2.3 *References*

[1] Matsushita, T. and Hashizume, H., 1983. X-ray Monochromators. Handbook on Synchrotron Radiation, 1, pp.261-314.
[2] Bragg, W.H. and Bragg, W.L., 1913. The reflection of X-rays by crystals. Proceedings of the Royal Society of London. Series A, Containing Papers of a Mathematical and Physical Character, 88(605), pp.428-438.
[3] Halliwell, M.A.G., Lyons, M.H. and Hill, M.J., 1984. The interpretation of X-ray rocking curves from III–V semiconductor device structures. Journal of crystal growth, 68(2), pp.523-531.

[4] Speriosu, V.S., Paine, B.M., Nicolet, M.A. and Glass, H.L., 1982. X-ray rocking curve study of Si-implanted GaAs, Si, and Ge. Applied Physics Letters, 40(7), pp.604-606.
[5] Masiello, F., Cembali, G., Chumakov, A.I., Connell, S.H., Ferrero, C., Härtwig, J., Sergeev, I. and Van Vaerenbergh, P., 2014. Rocking curve measurements revisited. Journal of Applied Crystallography, 47(4), pp.1304-1314.
[6] Authier, A., 2006. Dynamical theory of X-ray diffraction. International Tables for Crystallography, pp.626-646.
[7] Beaumont, J.H. and Hart, M., 1974. Multiple Bragg reflection monochromators for synchrotron X radiation. Journal of Physics E: Scientific Instruments, 7(10), p.823.
[8] Kirkpatrick, P. and Baez, A.V., 1948. Formation of optical images by X-rays. JOSA, 38(9), pp.766-774.
[9] Takeuchi, A., Suzuki, Y., Takano, H. and Terada, Y., 2005. Kirkpatrick-Baez type X-ray focusing mirror fabricated by the bent-polishing method. Review of scientific instruments, 76(9), p.093708.
[10] Liu, C., Conley, R., Assoufid, L., Cai, Z., Qian, J. and Macrander, A.T., 2004, May. From flat substrate to elliptical KB mirror by profile coating. In AIP Conference Proceedings (Vol. 705, No. 1, pp. 704-707). AIP.
[11] Thiess, H., Lasser, H. and Siewert, F., 2010. Fabrication of X-ray mirrors for synchrotron applications. Nuclear Instruments and Methods in Physics Research Section A: Accelerators, Spectrometers, Detectors and Associated Equipment, 616(2-3), pp.157-161.
[12] Mills, D., Padmore, H. and Lessner, E., 2013. X-ray optics for BES light source facilities. Brookhaven National Laboratory (BNL), Upton, NY (United States).
[13] Moeller, S., Arthur, J., Brachmann, A., Coffee, R., Decker, F.J., Ding, Y., Dowell, D., Edstrom, S., Emma, P., Feng, Y. and Fisher, A., 2011. Photon beamlines and diagnostics at LCLS. Nuclear Instruments and Methods in Physics Research Section A: Accelerators,

Spectrometers, Detectors and Associated Equipment, 635(1), pp.S6-S11.
[14] Baez, A.V., 1952. A study in diffraction microscopy with special reference to x-rays. JOSA, 42(10), pp.756-762.
[15] Aristov, V.V., Basov, Y.A., Kulipanov, G.N., Pindyurin, V.F., Snigirev, A.A. and Sokolov, A.S., 1989. Focusing properties of a Bragg-Fresnel lens in the white spectrum of synchrotron radiation. Nuclear Instruments and Methods in Physics Research Section A: Accelerators, Spectrometers, Detectors and Associated Equipment, 274(1-2), pp.390-393.
[16] Als-Nielsen, J. and McMorrow, D., 2011. Elements of modern X-ray physics. John Wiley & Sons.
[17] Snigirev, A., Kohn, V., Snigireva, I. and Lengeler, B., 1996. A compound refractive lens for focusing high-energy X-rays. Nature, 384(6604), p.49.
[18] Snigirev, A.A., Filseth, B., Elleaume, P., Klocke, T., Kohn, V., Lengeler, B., Snigireva, I., Souvorov, A. and Tuemmler, J., 1997, December. Refractive lenses for high-energy x-ray focusing. In High Heat Flux and Synchrotron Radiation Beamlines (Vol. 3151, pp. 164-170). International Society for Optics and Photonics.
[19] Tomie, T., Agency of Industrial Science, 1997. X-ray lens. U.S. Patent 5,594,773.
[20] Gary, C.K., 2013. Compound Refractive Lenses for Thermal Neutron Applications (No. DOE ADELPHI ER84991). Adelphi Technology, Inc..
[21] Eskildsen, M.R., Gammel, P.L., Isaacs, E.D., Detlefs, C., Mortensen, K. and Bishop, D.J., 1998. Compound refractive optics for the imaging and focusing of low-energy neutrons. Nature, 391(6667), p.563.
[22] Snigirev, A., Kohn, V., Snigireva, I., Souvorov, A. and Lengeler, B., 1998. Focusing high-energy x rays by compound refractive lenses. Applied optics, 37(4), pp.653-662.

[23] Beguiristain, H.R., Cremer, J.T., Piestrup, M.A., Gary, C.K. and Pantell, R.H., 2002. X-ray focusing with compound lenses made from beryllium. Optics letters, 27(9), pp.778-780.
[24] Andrejczuk, A., Nagamine, M., Sakurai, Y. and Itou, M., 2014. A planar parabolic refractive nickel lens for high-energy X-rays. Journal of synchrotron radiation, 21(1), pp.57-60.
[25] Artemev, A.N., Artemev, N.A., Kirillov, B.F., Kvardakov, V.V., Zabelin, A.V., Lastochkin, A.B., Maevsky, A.G., Naida, O.V., Dyatlov, A.A. and Stein, A.A., 2007. Development, production, and investigation of PMMA-based X-ray compound refractive lenses. Instruments and Experimental Techniques, 50(4), pp.539-542.
[26] Snigirev, A.A., Yunkin, V., Snigireva, I., Di Michiel, M., Drakopoulos, M., Kouznetsov, S., Shabel'nikov, L., Grigoriev, M., Ralchenko, V., Sychov, I. and Hoffmann, M., 2002, November. Diamond refractive lens for hard X-ray focusing. In Design and Microfabrication of Novel X-Ray Optics (Vol. 4783, pp. 1-9). International Society for Optics and Photonics.
[27] Kononenko, T.V., Ralchenko, V.G., Ashkinazi, E.E., Polikarpov, M., Ershov, P., Kuznetsov, S., Yunkin, V., Snigireva, I. and Konov, V.I., 2016. Fabrication of polycrystalline diamond refractive X-ray lens by femtosecond laser processing. Applied Physics A, 122(3), p.152.
[28] Terentyev, S., Polikarpov, M., Snigireva, I., Di Michiel, M., Zholudev, S., Yunkin, V., Kuznetsov, S., Blank, V. and Snigirev, A., 2017. Linear parabolic single-crystal diamond refractive lenses for synchrotron X-ray sources. Journal of synchrotron radiation, 24(1), pp.103-109.
[29] S. M. Blinder. "The Structure of Diamond". http://demonstrations.wolfram.com/TheStructureofDiamond/. Wolfram Demonstrations Project.
[30] Jayaraman, A., 1983. Diamond anvil cell and high-pressure physical investigations. Reviews of Modern Physics, 55(1), p.65.
[31] Zhang, Q., Polikarpov, M., Klimova, N., Larsen, H.B., Mathiesen, R., Emerich, H., Thorkildsen, G., Snigireva, I. and Snigirev, A., 2019.

Investigation of ‘glitches’ in the energy spectrum induced by single-crystal diamond compound X-ray refractive lenses. Journal of synchrotron radiation, 26(1), pp.109-118.
[32] Zhang, Q., Polikarpov, M., Klimova, N., Larsen, H.B., Mathiesen, R., Emerich, H., Thorkildsen, G., Snigireva, I. and Snigirev, A., 2019, January. Investigation of glitches induced by single-crystal diamond compound refractive lenses based on crystal orientation. In AIP Conference Proceedings (Vol. 2054, No. 1, p. 060007). AIP Publishing.
[33] Antipov, S., Baryshev, S.V., Butler, J.E., Antipova, O., Liu, Z. and Stoupin, S., 2016. Single-crystal diamond refractive lens for focusing X-rays in two dimensions. Journal of synchrotron radiation, 23(1), pp.163-168.
[34] Vaughan, G.B., Wright, J.P., Bytchkov, A., Rossat, M., Gleyzolle, H., Snigireva, I. and Snigirev, A., 2011. X-ray transfocators: focusing devices based on compound refractive lenses. Journal of synchrotron radiation, 18(2), pp.125-133.
[35] Narikovich, A., Barannikov, A., Ershov, P., Klimova, N., Lushnikov, A., Lyatun, I., Panormov, I., Polikarpov, M., Sinitsyn, A., Zverev, D. and Snigireva, I., 2018. Mini-transfocator for X-ray focusing and microscopy. Microscopy and Microanalysis, 24(S2), pp.294-295.
[36] Fu, M.L., Zhou, H.Q., Zhang, M., Quan, B.S., Wang, H., Mao, C.W., Wang, C.H. and Shen, X.Y., 2014. Design and fabrication of cascaded X-ray planar parabolic compound refractive lens. Acta Physica Sinica, 63(19), p.194103.
[37] Polikarpov, M., Snigireva, I. and Snigirev, A., 2014. X-ray harmonics rejection on third-generation synchrotron sources using compound refractive lenses. Journal of synchrotron radiation, 21(3), pp.484-487.
[38] Lengeler, B., Schroer, C., TuÈmmler, J., Benner, B., Richwin, M., Snigirev, A., Snigireva, I. and Drakopoulos, M., 1999. Imaging by parabolic refractive lenses in the hard X-ray range. Journal of Synchrotron Radiation, 6(6), pp.1153-1167.

[39] Lengeler, B., Schroer, C.G., Richwin, M., Tümmler, J., Drakopoulos, M., Snigirev, A. and Snigireva, I., 1999. A microscope for hard x rays based on parabolic compound refractive lenses. Applied physics letters, 74(26), pp.3924-3926.

3 Methodology

In the preceding chapters, different types of X-ray sources and beam conditioning devices (including monochromators and focusing optical devices) have been discussed in detail. The combination of both monochromators and focusing optics has already been successfully used in almost all SR-experiments. In this chapter, emphasis will be put on CRLs which are implemented as a transmission device for a wide energy range. In that context, for single-crystal diamond CRLs, different dips of intensity are observed at some specific energies shown in Fig. 20.

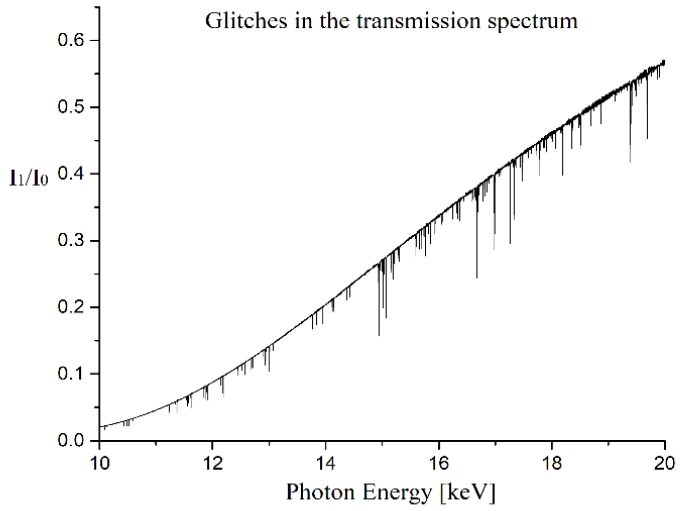

Figure 20 – "Glitch effects" as they appear in the transmission spectrum. I_0 is the intensity recorded by the ionization chamber before the sample, while I_1 refers to the intensity detected by the chamber after X-rays pass through CRLs. For this particular example, it clearly shows that there exists an energy window between 13.2 keV and 13.8 keV that is free from any glitches.

These drops of intensity resemble the hanging icicles on the branches of a tree and are simply named as "glitch effects". In the current thesis, it is already shown the operational principles of CRLs and the other major

task is to gain a deeper insight into the promising CRLs, particularly the influence of the glitches.

Previously, the research work done by Polikarpov *et al.* [1] reported to observe the occurrence of significant intensity drops in the spectrum when performing an energy scan experiment concluded that a call for a more rigorous treatment was necessary. The reason why this phenomenon should be investigated more thoroughly is that the loss of intensity will deteriorate the performance of some practical techniques, *e.g.* a poorer resolution for scanning transmission X-ray microscopy (STXM) [2] and scanning X-ray diffraction microscopy [3]. Therefore, it is imperative to deal with this issue as we want to avoid, minimize, or at least have an intuitive understanding of the mechanism of the glitches. In the first place, how some experimental factors, including those from the characteristics of the beam, sample stage, interactions of the beam and the sample deserve a comprehensive analysis. Secondly, owing to the use of single-crystal diamond, the glitches may be sensitive to the orientation. Information about the orientation of the sample with respect to the beam is extracted from the **UB** matrix (refer forward to Subchapter 3.2) and the positions and "strengths" of the glitches can be predicted by applying some specific extinction rules for diamond structure. This will help us determine the "energy window" without any glitches. To achieve these purposes, two distinct experiments were designed: an energy scanning experiment and ω-scan setup, respectively.

Before setting up the experiments, priority should be given to the selection of beamlines among all the existed beamlines at ESRF. BM31, being one of the two Swiss-Norwegian beamlines (SNBL) at ESRF, is specialized in high resolution powder diffraction (HRPD). The beamline is designed in a flexible way to measure XAS and HRPD or even a combination of both techniques on the samples under different experimental conditions (heating, cooling, in situ catalytic conditions *etc*.). The main characteristics of BM31 are listed on its homepage [4]: (1) a very wide incident energy range, from 4.9 keV to 70 keV; (2) 13-

element Germanium detector with fast digital multi-channel analyser electronics for XAS measurements at extremely low concentrations; (3) step-by-step data collection with down to 1s acquisition time; (4) fast monochromator scans with 'on-the-fly' date collection for fast X-ray absorption near edge absorption spectroscopy (XANES) measurements; (5) feedback on the second crystal of the monochromator to minimize other kind of “glitches” which are associated with the monochromator and originate from multi-beam diffraction events; (6) very rapid switching between two different monochromator modes - Si(111) and Si(311) and the flux delivered by Si(111) is three times more than that by Si(311). In addition, determination of single-crystal orientation may also be simply handled by placing an image plate detector (MAR345 detector [5]) in the downstream of an “add on” three-stage goniometer mounted at sample position. Combining the characteristics of the beamline and the requirements for the experiments, BM31 is suitable for performing XAS [6-8] experiments and determining the orientation of the single-crystal diamond lenses in alignment. A total of 9 shifts of beam time were granted for the proposed experiments and the backgrounds for the two experimental arrangements are given below:

3.1 *The energy scan experimental setup*

Considering CRLs’ principle of operation, it is essential to study its transmission spectrum (a plot of normalized intensity versus energy). This involves the same overall principles as for X-ray absorption spectroscopy (XAS) technique that is aimed at determining the local geometric and/or electronic structure of the samples. By now, XAS has been exploited in different fields, such as amorphous solids [9], solid solutions [10], catalysis [11], *etc*.

A schematic representation of XAS experiment is shown in Fig. 21 and its purpose is to measure the linear absorption coefficient as a function of X-rays’ incident energy by making use of the key components - ionization chambers [12]: one being placed before and the other being

installed right after the sample. As the name indicates, ionization chambers are gas-filled radiation detectors and the incident radiation may ionize the gas and create ion pairs within a gas. Then the charge from the number of ion pairs is captured and measured by the chamber and the intensity is recorded.

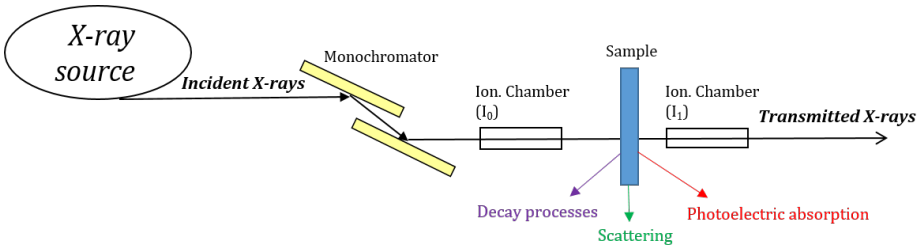

Figure 21 – A typical example of XAFS experiment setup. "Ion. Chamber" in the figure refers to the ionization chamber used for detection and measurement of X-ray radiation. In general, XAS involves transmission, photoelectric absorption, scattering (Compton and Thomson scattering) and decay (fluorescence and Auger electrons) processes.

Based on this, we can thus set up the energy scan experiment (Fig. 22) by mimicking that for XAFS. The energy range is set between 10 keV and 20 keV with an interval of 1eV by tuning the monochromator and it is achieved by taking advantage of piezo effect.

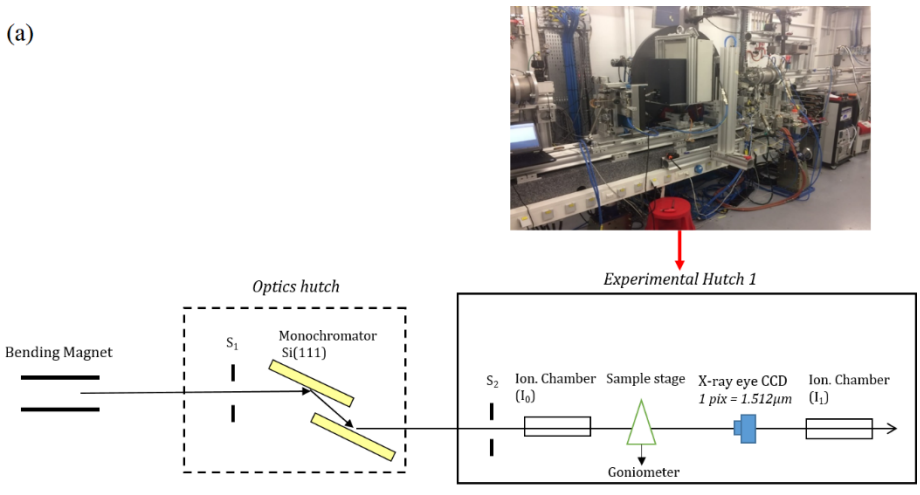

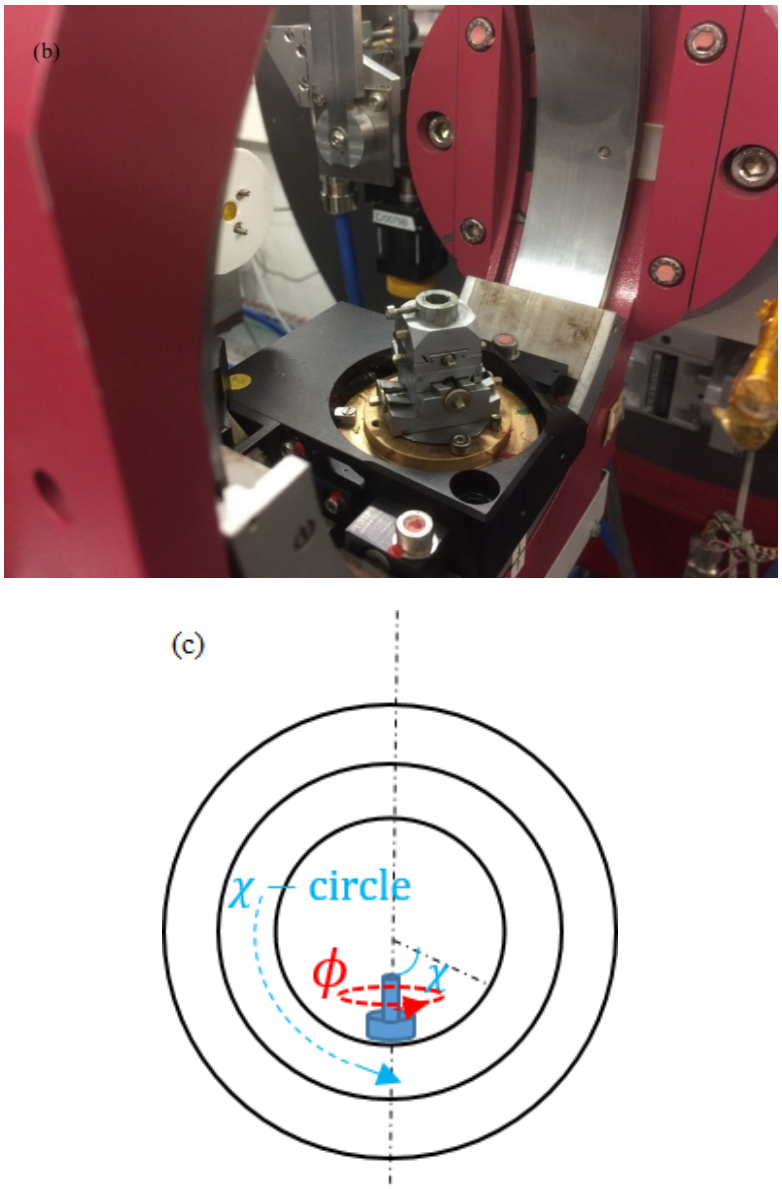

Figure 22 – (a) is an illustration of the experimental setup at BM31, ESRF to obtain the energy spectra of CRLs; (b) is a photo of the goniometer at the sample stage; (c) is the view of χ-circle from the X-ray source in Eulerian geometry with $\omega = 0°$: the ω-angle, which rotates about an axis perpendicular to X-ray beam and the φ-angle about the loop axis.

From the experimental setup point of view, a crucial question is to investigate to what extent experimental factors may influence the glitch patterns. First of all, the beam divergence may play a role. To study its effect, a condenser is placed in the very front end of the experimental hutch to change the beam divergence of the incident X-ray beam onto the sample. Secondly, the χ-angle setting in the illustration could also be counted as an influential factor and varying χ-angle is done via a motorized sample stage. Lastly, X-rays are very sensitive to the thickness of CRLs. In that context, one should note that for glass lenses used to focus visible light, the parameter – effective aperture is the same as its physical aperture; however, attenuation plays a vital role within X-rays' energy range and it is necessary to introduce the concept of effective aperture [13]. In the case of X-rays, the effective aperture is smaller than the physical aperture and is usually defined as the size of the aperture when the transmission function reduces to $\exp(-1)$. In other words, this means that the edges of CRLs absorb more intensity compared with the central part and different interacting positions of X-rays with the sample lenses are likely to affect the glitches, more accurately, strengths of the glitches.

By comparing the spectra with various beam divergences, χ-angles and interactive positions, we are capable of investigating the influence of the above mentioned experimental features on the glitches. These results will be presented in the forthcoming publications in Chapter 5.

3.2 *The experimental setup of ω-scan*

The aim of the second experimental arrangement is to deal with study of orientation of single-crystal diamond CRLs with respect to the beam, because the single-crystal orientation will significantly influence CRLs' performance. As we know, the orientation of the single-crystal determines different physical properties, including optical (spectral transmission), thermal (conductivity, expansion, *etc*.), mechanical

(hardness, radiation resistance) and electrical properties (dielectric and piezoelectric), *etc*.

The above mentioned glitch effects have a number of contributions, such as two-beam Bragg diffraction, multiple beam diffraction effects and beam divergence, *etc*. As a first approach, we suppose that the presence of the glitches in the energy spectrum is mainly owing to the fact that Bragg condition is satisfied at some specific energies when the energy changes continuously, namely, standard "two-beam Bragg diffraction". The description of sample orientation with respect to the incident X-ray radiation by means of the so-called "orientation matrix" or the "**UB** matrix" [14-16], is also of great importance because it may help us predict the positions of the glitches in terms of energy. Therefore, one needs to calculate the orientation matrix, which is in fact the product of two matrices, the orthogonal rotation matrix **U** and the orthonormalization matrix **B**, respectively. The **B** matrix is an upper triangle matrix which contains information about the unit cell parameters. In a systematic scanning process, the most convenient way of constructing the orthonormal coordinate system is to let its x-axis coincide with the reciprocal unit cell vector $\boldsymbol{a}^*$. The y-axis is then defined so that it lies in the $\boldsymbol{a}^*\boldsymbol{b}^*$ plane and is perpendicular to x -axis at the same time. The z-axis is chosen to complete a right-handed Cartesian system, which means it is perpendicular to $\boldsymbol{a}^*\boldsymbol{b}^*$ plane. Essentially, the **B** matrix specifies the components of unit cell of reciprocal lattice in the Cartesian laboratory coordinate system and is expressed as:

$$\mathbf{B} = \begin{bmatrix} a^* & b^*\cos\gamma^* & c^*\cos\beta^* \\ 0 & b^*\sin\gamma^* & -c^*\sin\beta^*\frac{\cos\beta^*\cos\gamma^*-\cos\alpha^*}{\sin\beta^*\sin\gamma^*} \\ 0 & 0 & c^* \end{bmatrix} \tag{3.1}$$

a^*, b^*, c^* are the conventional reciprocal lattice parameters and α^*, β^*, γ^* are the included angles between $\boldsymbol{b}^*$ and $\boldsymbol{c}^*$, $\boldsymbol{c}^*$ and $\boldsymbol{a}^*$, $\boldsymbol{a}^*$ and $\boldsymbol{b}^*$, respectively. The diamond has a cubic lattice structure in direct space, so it will certainly possess a cubic lattice in reciprocal space based on the

definition of reciprocity. Therefore, the **B** matrix for diamond is simplified to:

$$\mathbf{B} = \begin{bmatrix} a^* & 0 & 0 \\ 0 & b^* & 0 \\ 0 & 0 & c^* \end{bmatrix} \tag{3.2}$$

The function of **B** matrix is to transform from the reciprocal lattice vector, denoted as **h**, to the Cartesian coordinate system with respect to the crystal and could be described by the following formula: $\mathbf{h_c} = \mathbf{Bh}$, where $\mathbf{h_c}$ is the scattering vector in the crystal Cartesian system and characterizes a vector normal to a family of crystal lattice planes **h**. The relationship between the laboratory coordinate and the plane of the detector is given in Fig. 23.

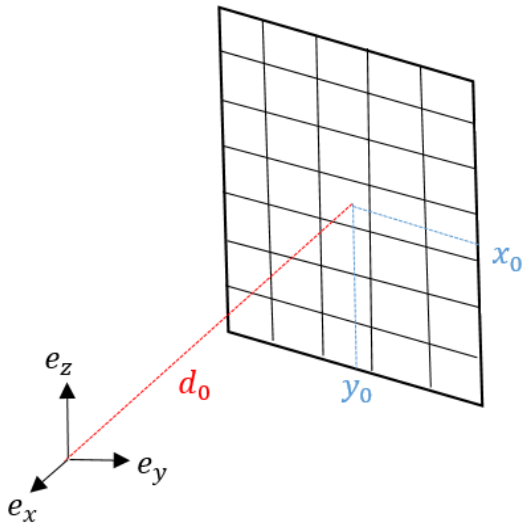

Figure 23 – The laboratory coordinate system and the plane of detector. In this case, the incoming beam intersects the plane of detector at the position of $\{x_0, y_0\}$ with d_0 being the crystal-to-detector distance.

Moreover, for the purpose of finding the Bragg reflections induced by these planes, another rotation matrix, denoted as the **U** matrix, is also needed. The **U** matrix is an orthogonal rotation matrix ($\mathbf{U}^{\mathrm{T}} = \mathbf{U}^{-1}$), which transforms from the orthonormal coordinate system attached to

the crystal to another Cartesian coordinate attached to the laboratory system.

In essence, the **UB** matrix acts on a reciprocal lattice vector **h** and brings it to be coincident with the scattering vector:

$$\mathbf{Q}_i = \mathbf{U}\mathbf{h}_{\mathbf{c}i} = \mathbf{UB}\mathbf{h}_i,\ i=1,2 \tag{3.3}$$

In this equation, the subscript i is used to distinguish two classes of Bragg reflections that are produced by non-parallel lattice planes.

Then it comes to the methodology of computing the **UB** matrix. As we know, the rotation of a crystal illuminated by a monochromatic X-ray beam forces its reciprocal lattice points to cross the surface of the so-called "Ewald sphere" [17]. Whenever this happens, a diffracted beam is originated in the center of the Ewald sphere and passes through the reciprocal point that lies on the Ewald spherical surface. Under these circumstances, the Bragg's law is fulfilled and the set of all diffracted beams will constitute the diffraction pattern, which can be captured and recorded by the detector. A 2D pixel detector provides a unique possibility to visual and record Bragg reflections from a crystalline system and thus we chose the well-known MAR345 area detector. In this way, a series of frames could be collected by mounting the sample lenses on the motorized sample stage (*cf.* Fig. 24). In this experimental setup, the usage of the area detector allows to collect diffracted X-ray beams over a wide solid angle. Due to the accessibility of the area detector, it is not necessary to choose a four-circle goniometer and a single rotating axis is enough. The **UB** matrix is obtained by setting up the systematic ω-scan with a positive ω-rotation pointing outwards in Fig. 3.3(c) when viewed from the X-ray source. During the rotation process, the wavelength is kept fixed and the monochromator is thus tuned as a stationary mono.

One may wonder that this setup is almost the same as that used for the wavelength calibration process (*cf.* Appendix 1). The only difference

between these two lies in the samples: the wavelength calibration experiment employs a polycrystalline standard reference material (LaB_6 powder in this case) to produce a set of concentric lines, while in the ω-scan setup here the single-crystal diamond CRLs is mounted on the goniometer. One should realize that since an X-ray CCD camera is in the beam path, a limited angular range should be set with caution to avoid collision. By trial and error, the angular range for ω-angle is set to start from $-49°$ to $20°$ with an interval of $\Delta\omega = 1°$. Thus we are able to collect a finite set of frames and collection of each frame takes approximately 10 minutes, including collecting and reading out time by the laser.

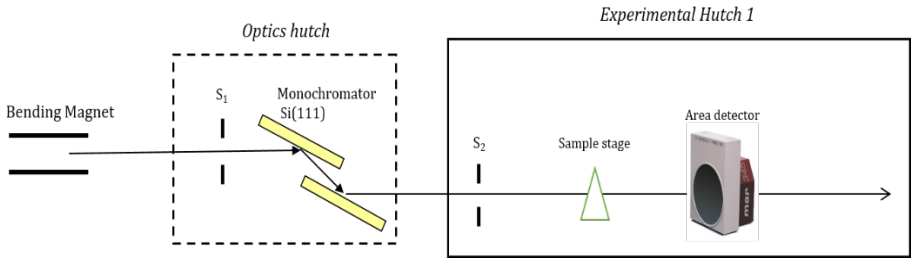

Figure 24 – The experimental setup of ω-scan. The 3-circle goniometer is mounted at the sample stage to quantitatively measure the rotation angle.

3.3 *Data processing*

The data obtained from the experiment should be processed for accurate analysis and a detailed description of the methods is given in the following:

3.3.1 Data processing for the energy scan experiment

When it comes to the data processing, XAS deals with measurement of absorption coefficient as a function of photon energy. The number of X-ray photons that are transmitted through a sample (I_1) is equal to the number of X-ray photons that are incident onto the sample (I_0) multiplied by a decreasing exponential with a factor of μt, usually expressed as:

$\ln(I_1/I_0) = -\mu t$, μ and t represent the absorption coefficient and the thickness of the sample, respectively. Likewise, data handling of the energy scan experiment can be done in a similar way, but one should note that the glitches from the multiple beam induced monochromator should be eliminated in the final glitch pattern of CRLs. The steps are summarized as follows: first, we divided I_1 by I_0 (I_1 / I_0) as a function of the incident energy and mask all the glitches in this data column. Then a low order polynomial (1 or 2, max 3) was fitted through the remaining I_1 / I_0 line to mark the 100% reference line and then the drops of the glitches are then given in percent with respect to that baseline.

3.3.2 Data processing for ω-scan setup

Due to the actual sample-to-detector distance and the small unit cell dimensions, only a very small number of accessible reflections at such low 2θ angles and we had to manually select those frames with relatively brighter diffraction spots in order to determine the orientation matrix as precisely as possible.

The pixel positions of the incoming beam and the Bragg reflection spots were read out using the software – *CrysAlis* [18]. Special care should be taken as the pixels of the incoming beam (x_0, y_0) and the diffracted spots (x, y) are normally measured by pixel numbers, while the sample-to-detector distance is measured in mm. In general cases, the distance between the transmitted beam centre and the Bragg reflections are obtained by multiplying the numbers of pixels in between and the size of the pixel, and the distance is then converted to the unit of mm. It is also important to note that Bragg reflections are also represented by the frame numbers and they should be recorded with caution because a wrong ω-angle may bring in errors in calculating the **UB** matrix. By making use of the geometrical setting, the first task was to determine the classes these reflections belong to, as is shown in Fig. 25.

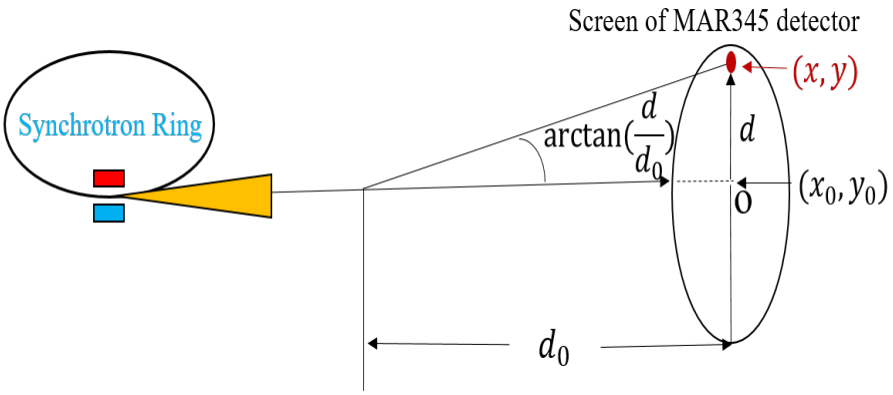

Figure 25 – An illustration on how to calculate the half cone angle, the red dot represents the Bragg spot. Here d characterizes the distance from the beam stop to the diffracted spots and d_0 is the sample-to-detector distance.

In the actual experimental setup, we retrieved the effective frames (*cf.* Fig. 26) with the calculated 2θ angles as such:

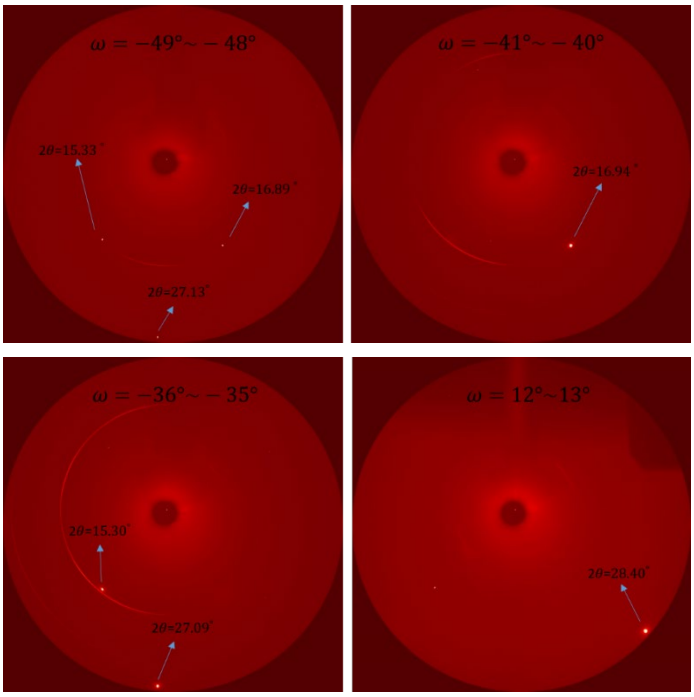

Figure 26 – The effective diffraction frames collected from ω-scan.

To show explicit implications of the **UB** matrix, the concept of Ewald construction is useful. The wavevector of the incident X-ray radiation $\mathbf{k}_0$ is parallel to x-axis and the outgoing wavevector is parallel to $\mathbf{k}_\mathrm{f}$, the scattering vector $\mathbf{Q}_i$ is defined as: $\mathbf{Q}_i = \mathbf{k}_\mathrm{f} - \mathbf{k}_0$, shown in Figure 27. An arbitrary reciprocal lattice node is expressed as:

$$\mathbf{H}_{hkl} = h\mathbf{a}^* + k\mathbf{b}^* + l\mathbf{c}^* \tag{3.4}$$

where h, k, l are Miller indices. The Bragg condition is satisfied when the scattering vector is equal to the reciprocal lattice vector, *i.e.* $\mathbf{H}_{hkl} = \mathbf{Q}_i$. For the convenience of further calculation, we will define an alignment vector, which is denoted as $\mathbf{g_0}$ and is expressed as: $\mathbf{g_0} = -\mathbf{k}_0 = [-1\ 0\ 0\ ]$ in the ideal case. However, the actual incoming beam $\mathbf{k}'$ may deviate slightly from the ideal unit vector of the incoming beam $\mathbf{g}_0$ under real experimental configuration, as is depicted in Fig. 27.

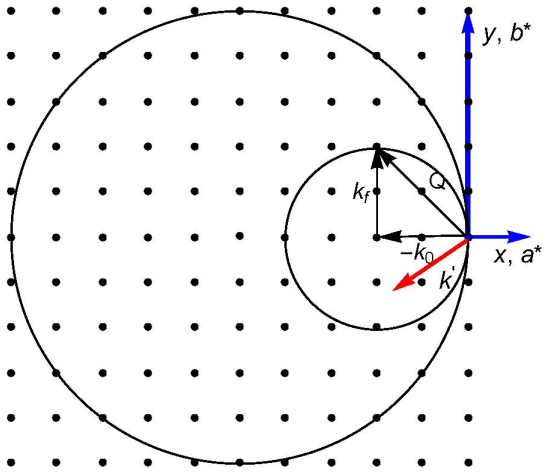

Figure 27 – The illustration of Ewald sphere with the radius of $1/\lambda$ for the energy scan, where λ is the wavelength of X-ray radiation. According to the relation between the energy E and the wavelength: $E = h\nu = h\frac{c}{\lambda}$, the radius of the Ewald sphere is proportional to the energy. Therefore, the internal circle corresponds to the minimum energy and the outer circle correspond to the maximum energy. $-\mathbf{k}_0$ characterizes the direction of ideal alignment while $\mathbf{k}'$ (the red arrow) characterizes the actual alignment and it happens that the real alignment deviates from the ideal case.

Before performing further calculations, let us recall the Bragg equation:

$$2d_{hkl}\sin\theta = n\lambda \tag{3.5}$$

where n is an integer (not to be confused with index of refraction), d_{hkl} is the lattice spacing and is equal to $d_{hkl} = \frac{a}{\sqrt{h^2+k^2+l^2}}$ for a cubic lattice, θ is the angle between the incident beam and the family of lattice planes with Miller indices h, k, l. Diamond is in the $\mathrm{Fd\bar{3}m}$ space group and has the face-centered cubic Bravais lattice. This means the allowed reflections should satisfy the condition that all Miller indices are odd, or even with $h + k + l = 4m$ (m is an integer); otherwise, they are the so-called forbidden reflections due to extinction phenomenon. This selection principle is very useful for predicting the glitches because it removes the forbidden reflections. By inspecting the frames in this specific case, two types of reflections are observed and they should come from the lattice planes with two lowest 2θ-angles, namely, {111} and {220} respectively. However, this should be verified by comparing the theoretical and actual 2θ -angles. The theoretical 2θ -angles are completely determined from Bragg equation, recast in the form:

$$2\theta = 2\sin^{-1}(\frac{\lambda}{2a}\|\mathbf{h}\|) \tag{3.6}$$

where $\|\mathbf{h}\|$ is the norm of $\mathbf{h}$ and the other symbols have their usual meanings. In crystallography and materials science, the term "metric" is used to indicate that the metric tensor pertains to the measurement properties of the space. As mentioned before, the sample-to-detector distance and the pixel size of MAR345 detector are already known, we are able to define the measurement metric (denoted as **M**). Followed by that, the metric **B** is then obtained by performing Cholesky decomposition on the metric **M**. Then we are able to construct the unit vector along the incoming beam $\boldsymbol{s}_0$, as well as the diffracted beam directions $\boldsymbol{s}_\mathrm{h}(x, y)$:

$$\boldsymbol{s}_0 = [-1\ 0\ 0],$$

$$\boldsymbol{s}_{\mathrm{h}}(x,y) = \frac{\mathbf{B}\cdot[-d_0,\ x-x_0,\ y-y_0]}{\sqrt{[-d_0,\ x-x_0,\ y-y_0]\cdot\mathbf{M}\cdot[-d_0,\ x-x_0,\ y-y_0]}} \tag{3.7}$$

where d_0 represents the sample-to-detector distance, (x_0, y_0) and (x, y) have the same meanings as that in Eqn. positions of the direct beam (beam center) on the pixel-detector screen. By substituting all the instrumental parameters into Eqn. (3.7), the actual 2θ-angles can be computed and the types of reflections in principle can be determined. Another implication of $\boldsymbol{s}_0$ and $\boldsymbol{s}_{\mathrm{h}}(x,y)$ is to determine the coordinates of the reciprocal lattice nodes in the Cartesian coordinate system with respect to the crystal. ω-angles associated with the effective frames having sharp reflections are used here to compute **U** matrix. An ω-rotation matrix **R** is also needed:

$$\mathbf{R}(\omega_i) = \begin{bmatrix} \cos\omega_i & -\sin\omega_i & 0 \\ \sin\omega_i & \cos\omega_i & 0 \\ 0 & 0 & 1 \end{bmatrix}, i=1, 2 \tag{3.8}$$

ω_i represents the corresponding ω-angles where the Bragg reflections are captured. Then the coordinates of the reciprocal lattice nodes are expressed as:

$$\mathbf{v}_i = \mathbf{R}(\omega_i)\cdot(\boldsymbol{s}_{\mathrm{h}}(x,y) - \boldsymbol{s}_0),\ i=1, 2 \tag{3.9}$$

In general, two slightly different methods can be implemented to calculate the **UB** matrix (the codes for these two methods in *Mathematica* are given in Appendix 2): (i) two independent reflections with known parameters of the lattice structure, and (ii) three accessible non-parallel Bragg reflections with unknown lattice parameters. In the present case, we know all the lattice parameters to an adequate precision and that is why the approach (i) is exclusively used, but the approach (ii) is also very useful especially when one wants to deduce the lattice parameters of an unknown material from the metric tensor. It turns out that both two methods lead to very similar results, *cf.* Appendix 2. The combined use of these parameters will provide an estimation of the **UB**

matrix for this sample. Here we briefly review the derivations. Ideally, Eqn. (3.3) should be satisfied. However, due to uncertainties in the angular measurements and lattice parameters, a right-handed set of orthogonal unit vectors, $\mathbf{t}_{c1}$, $\mathbf{t}_{c2}$, $\mathbf{t}_{c3}$, in the Cartesian system with respect to the crystal are defined such that $\mathbf{t}_{c1}$ is parallel to $\mathbf{h}_{c1}$; $\mathbf{t}_{c2}$ lies in the plane of $\mathbf{h}_{c1}$ and $\mathbf{h}_{c2}$, and can be seen as the normalized cross product of $\mathbf{h}_{c1}$ and $\mathbf{h}_{c2}$; $\mathbf{t}_{c3}$ is perpendicular to the planes of $\mathbf{t}_{c1}$, $\mathbf{t}_{c2}$. Another triple, $\mathbf{t}_{\varphi 1}$, $\mathbf{t}_{\varphi 2}$ and $\mathbf{t}_{\varphi 3}$, based on observations are defined in the same way as $\mathbf{t}_{c1}$, $\mathbf{t}_{c2}$, $\mathbf{t}_{c3}$, simply by replacing $\mathbf{h}_i$ with $\mathbf{v}_i$ (i=1, 2). The orthogonal rotation matrix $\mathbf{U}$ is defined such that:

$$\mathbf{t}_{\varphi j} = \mathbf{U}\,\mathbf{t}_{cj}, \quad j = 1,2,3 \tag{3.10}$$

Since $\mathbf{t}_{cj}$ are orthogonal, the $\mathbf{U}$ matrix is deduced to be:

$$\begin{aligned}\mathbf{U} &= \left[\mathbf{t}_{\varphi 1}, \mathbf{t}_{\varphi 2}, \mathbf{t}_{\varphi 3}\right]^{-1} \cdot \left[\mathbf{t}_{c1}, \mathbf{t}_{c2}, \mathbf{t}_{c3}\right] \\ &= \left[\mathbf{t}_{\varphi 1}, \mathbf{t}_{\varphi 2}, \mathbf{t}_{\varphi 3}\right]^{\mathrm{T}} \cdot \left[\mathbf{t}_{c1}, \mathbf{t}_{c2}, \mathbf{t}_{c3}\right]\end{aligned} \tag{3.11}$$

By multiplying the $\mathbf{U}$ matrix with the $\mathbf{B}$ matrix, the $\mathbf{UB}$ matrix is then readily obtained.

The single-crystal diamond CRLs in this experiment has $\pm$ 3° miscut uncertainty, which means that the real alignment $\mathbf{g}$ (differ from the assumed ideally perfect alignment $\mathbf{g_0}$) should be introduced to characterize the orientation of [-1 0 0] in the laboratory system quantitatively and it is denoted as:

$$\mathbf{g} = \frac{\mathbf{UB}\cdot[-1\ 0\ 0]}{\|\mathbf{UB}\cdot[-1\ 0\ 0]\|} \tag{3.12}$$

The X-ray energy leading to Bragg diffraction is then expressed as:

$$\mathrm{E[keV]} = \frac{12.398}{\lambda[\text{Å}]} = 12.398 \times \left(\frac{-2\mathbf{g}\cdot\mathbf{G^{-1}}\cdot\mathbf{h}}{\sqrt{\mathbf{g}\cdot\mathbf{G^{-1}}\cdot\mathbf{g}\,\mathbf{h}\cdot\mathbf{G^{-1}}\cdot\mathbf{h}}}\right)^{-1} \tag{3.13}$$

where $\mathbf{h} = [h\ k\ l]$ represents the coordinate matrix, $\mathbf{G^{-1}}$ is the reciprocal metric tensor. By taking into account the extinct reflections for diamond and at the same time neglecting negative energy solutions, we are capable of predicting the energy positions of the glitches. Regarding the prediction of the strengths of glitches, the kinematical diffraction theory [19] may in a first consideration be sufficient, and the glitch strengths can be obtained by multiplying the structure factor and the corresponding multiplicity factor (due to symmetry).

The spectrum retrieved from the energy scan is used as a benchmark for comparison and the spectra with varying experimental factors have been presented and analyzed in the publications (Chapter 5). Moreover, the method on predicting the glitches based on the kinematical theory of X-ray's diffraction is also discussed in detail. To sum up, the combined use of these two experimental setups investigates CRLs from two aspects: the possible experimental characteristics and the sample itself based on crystallography.

3.4 *References*

[1] Polikarpov, M., Emerich, H., Klimova, N., Snigireva, I., Savin, V. and Snigirev, A., 2018. Spectral X-Ray Glitches in Monocrystalline Diamond Refractive Lenses. Physica Status Solidi (b), 255(1), p.1700229.

[2] Jacobsen, C., Williams, S., Anderson, E., Browne, M.T., Buckley, C.J., Kern, D., Kirz, J., Rivers, M. and Zhang, X., 1991. Diffraction-limited imaging in a scanning transmission x-ray microscope. Optics Communications, 86(3-4), pp.351-364.

[3] Thibault, P., Dierolf, M., Menzel, A., Bunk, O., David, C. and Pfeiffer, F., 2008. High-resolution scanning x-ray diffraction microscopy. Science, 321(5887), pp.379-382.

[4]http://www.esrf.eu/fr/home/UsersAndScience/Experiments/CRG/BM01/bm31.html.

[5] Muchmore, S.W., 1999. Experiences with CCD detectors on a home X-ray source. Acta Crystallographica Section D: Biological Crystallography, 55(10), pp.1669-1671.
[6] Koningsberger, D.C. and Prins, R., 1988. X-ray absorption: principles, applications, techniques of EXAFS, SEXAFS, and XANES.
[7] Yano, J. and Yachandra, V.K., 2009. X-ray absorption spectroscopy. Photosynthesis research, 102(2-3), p.241.
[8] Van Bokhoven, J.A. and Lamberti, C. eds., 2016. X-ray absorption and X-ray emission spectroscopy: theory and applications (Vol. 1). John Wiley & Sons.
[9] Qamar, A., LeBlanc, K., Semeniuk, O., Reznik, A., Lin, J., Pan, Y. and Moewes, A., 2017. X-ray spectroscopic study of amorphous and polycrystalline PbO films, α-PbO, and β-PbO for direct conversion imaging. Scientific reports, 7(1), p.13159.
[10] Bao, H., Qian, K., Chen, X., Fang, J. and Huang, W., 2019. Spectroscopic study of microstructure-reducibility relation of CexZr1−xO2 solid solutions. Applied Surface Science, 467, pp.361-369.
[11] Lomachenko, K.A., Borfecchia, E., Negri, C., Berlier, G., Lamberti, C., Beato, P., Falsig, H. and Bordiga, S., 2016. The Cu-CHA deNO x catalyst in action: temperature-dependent NH3-assisted selective catalytic reduction monitored by operando XAS and XES. Journal of the American Chemical Society, 138(37), pp.12025-12028.
[12] Pruitt, J.S. and Domen, S.R., 1962. Determination of total X-ray beam energy with a calibrated ionization chamber (Vol. 48). US Department of Commerce, National Bureau of Standards.
[13] Lengeler, B., Schroer, C., Tümmler, J., Benner, B., Richwin, M., Snigirev, A., Snigireva, I. and Drakopoulos, M., 1999. Imaging by parabolic refractive lenses in the hard X-ray range. Journal of Synchrotron Radiation, 6(6), pp.1153-1167.
[14] Busing, W.R. and Levy, H.A., 1967. Angle calculations for 3-and 4-circle X-ray and neutron diffractometers. Acta Crystallographica, 22(4), pp.457-464.

[15] Messerschmidt, A.T. and Pflugrath, J.W., 1987. Crystal orientation and X-ray pattern prediction routines for area-detector diffractometer systems in macromolecular crystallography. Journal of Applied Crystallography, 20(4), pp.306-315.
[16] Yashiro, W., Kusano, S. and Miki, K., 2005. Determination of crystal orientation by an area-detector image for surface X-ray diffraction. Journal of applied crystallography, 38(2), pp.319-323.
[17] Loh, Y.L., 2017. The Ewald sphere construction for radiation, scattering, and diffraction. American Journal of Physics, 85(4), pp.277-288.
[18] CrysAlis, C.C.D., 2008. CrysAlis Red. Xcalibur PX Software, Oxford Diffraction Ltd., Abingdon, England.
[19] Baake, M. and Grimm, U., 2011. Kinematic diffraction from a mathematical viewpoint. Zeitschrift für Kristallographie Crystalline Materials, 226(9), pp.711-725.

4 Investigation of single-crystal diamond 2D half lens in symmetrical Laue case

Abstract

A focused X-ray beam is always desired for almost all experiments. This has led to the revival of X-ray optics, or more specifically, focusing optics. Compound refractive lenses (CRLs), being a type of X-ray focusing elements, first proposed in 1990s by taking advantage of refractive effect and have been experimentally verified to effectively focus X-ray radiation. Soon after that, some advanced versions based on the prototype were fabricated, among which, a single 2D half lens made of single-crystal diamond. This is quite promising because it is generally believed to possess great potentials, especially being implemented as a front-end device. In the present analysis, however, we assume, for simplicity, an X-ray lab source and focusing element in terms of a perfect crystal. In the (reference) case of a flat crystal, the simulation shows that the intensity of the refracted and diffracted beams are complementary, and the intensity distribution is sensitive to the thickness as well. However, in terms of a concave entrance surface, we can replace the curved surface with staircase-like approximation. The results can be further classified into two cases: non-interference column propagation and incoherent addition of intensity. Literally, the former one is adopted for the case where the induced Borrmann triangle propagates independently along each column. This is provided that the lateral width of the triangle is narrow. In the case of wider Bormann triangles, the total intensity distribution may be added incoherently and the simulation result shows that the smaller the curvature radius is, the better the focusing effect is obtained.

Key words:

Single 2D half lens, symmetrical Laue case, intensity distribution.

4.1 *Introduction*

It is known that the most fascinating feature of X-ray radiation is the ability to make the "invisible" matter visible due to its extremely short wavelength, which is typically of the order of 10^{-10}m. Nowadays, two mainstream mechanisms are often employed to generate X-ray radiation: one is conventional X-ray tubes (also referred to as X-ray lab source) owing to its ease of accessibility and portability; the other one is synchrotron radiation (SR) light source which can produce extremely brilliant X-rays (many orders higher than the former X-ray tube). Despite this, most of the current SR facilities belong to the third generation and the next generation source - X-ray free electron lasers (XFELs) [1-3] that pursues even better coherence and brilliance are already being under construction and in operation worldwide.

In parallel to the continuous improvement of X-ray sources, a variety of X-ray optical devices are often implemented to modify X-ray beam as desired. For example, a quasi-monochromatic beam with higher intensity at the focal spot is always wanted for most experimental techniques. In consequence, this drives the development of X-ray beam conditioning devices, including both monochromators and focusing devices. Since the sample lens investigated in this paper is a type of X-ray focusing device, the emphasis of the description will thus be put there. Literally, the ultimate purpose of X-ray focusing devices is to obtain a smaller focus with higher intensity. In analogy with focusing visible light, the first attempt to focus X-rays was made by Röntgen himself using a prism, but he failed due to the extremely weak refraction effect. Afterwards, it was considered impossible to focus the radiation until Kirkpatrick & Baez designed the X-ray mirror (also known as "K-B mirrors" to honor their contribution) [4-6] for X-ray microscope in 1948. Nowadays, in addition to X-ray mirrors, Bragg-Fresnel lenses [7, 8], capillary lens [9, 10], multilayer Laue lenses (MLL) [11, 12] and compound refractive lenses (CRLs) [13, 14] are often used in different experimental setups. Compared with other focusing elements, CRLs have some prominent

advantages, such as compactness and ease of alignment, and they have thus been installed at almost all the synchrotron facilities for X-ray microscope [15] and high resolution X-ray imaging experiments [16]. Regarding the selection of suitable materials, those with low atomic elements are favored in order to minimize the absorption effect, but other aspects of the material should also be taken into consideration: beryllium [17], for instance, may cause diffuse scattering because it is available mainly in the form of a sintered structure and may also arouse environmental concerns because of its toxicity. Nickel [18] is particularly ideal for relatively high energy X-rays (above 100 keV); diamond is considered suitable owing to very stable physical properties especially when the lenses are expected to be exposed to intense synchrotron radiation for a long time. In general, diamond CRLs can be classified into two categories: polycrystalline and single-crystal diamond CRLs. Comparatively speaking, the focusing effect of polycrystalline lenses turns out to be worse than theoretical estimations [19]. This is because the actual shape of the entrance surface may deviate from the ideal parabolic surface during the femtosecond laser machining process and the grain boundaries can also yield diffuse scattering, leading to a poorer focusing performance. However, single-crystal or monocrystalline diamond [20] is free from this negative effect and has thus been chosen as an alternative to fabricate CRLs.

Recently, a new type 2D half lens with a rotational symmetric geometrical structure has been proposed and it is predicted to have a promising future, especially in front-end applications, such as being installed as a pre-collimating and beam-shaping optics [21]. The desired 2D half lens profile of the paraboloid can achieve higher revolution compared with the planar lenses [22]. The investigation on the dynamical transmission in CRLs will help us gain insight into the interplay between the transmitted and diffracted beams. The intensity distribution of the transmitted beam is of particular interest because it can describe the focusing effect, which is a key factor in evaluating CRLs' performance.

In addition, 2D half lens has only one curved surface and is deemed to be a very good starting point when one wants to obtain insight into a more complicated case – biconcave lenses in the future. Therefore, this 2D half lens deserves a rigorous treatment.

4.2 *The sample - 2D half lens*

The 2D half lens was polished out of a high-quality synthetic single-crystal diamond plate using laser micro-machining technique [23]. Based on the theory of geometrical optics, the entrance surface of this lens is chosen to be parabolic in order to avoid spherical aberration as much as possible, as is shown in Fig. 28.

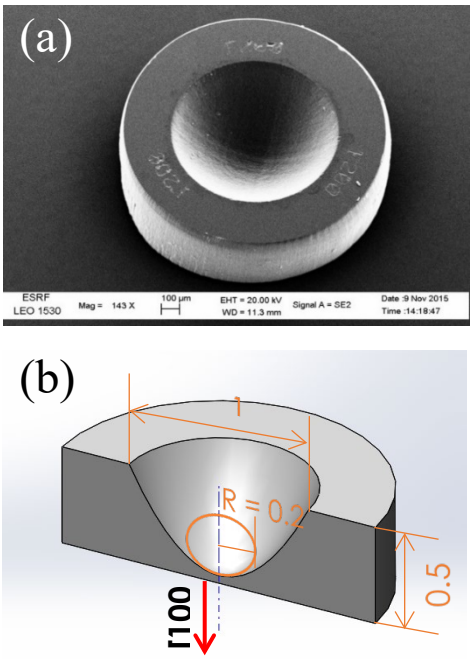

Figure 28 – (a) is a scanning electron microscopic (SEM) image taken at ESRF and (b) is a schematic drawing of the sample half lens. It has been marked that the geometrical aperture of the half lens is 1 mm, the curvature radius at the parabola is 200 μm, the thickness of the plate is 500 μm and the center thickness is 30 μm [22].

After setting up the energy scan experiment [24] at BM31 station, European Synchrotron Radiation Facility (ESRF), the energy spectrum

(*cf.* Fig. 29) of the 2D half lens between 10 keV and 20 keV is retrieved and for better inspection, the energy spectrum range from 16 keV to 18 keV with finer step width is also attached.

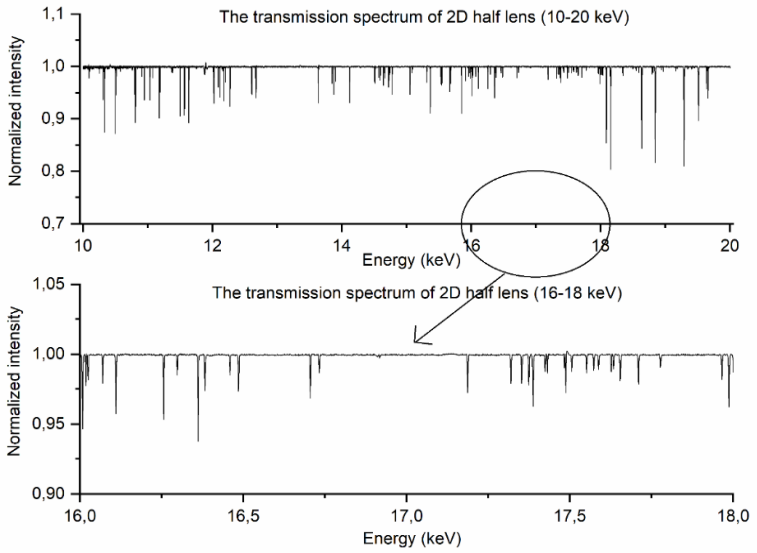

Figure 29 – The energy spectrum for a single 2D half lens obtained from the energy scan experiment set up at ESRF; top: the energy spectrum with a range from 10 keV to 20 keV, bottom: the spectrum between 16 keV and 18 keV with a finer step width.

It can be seen from Fig. 29 that some drops of intensity (vividly called 'glitches') appear at certain specific energies in the spectrum and the most significant one can even reach up to approximately 20 percent. As a matter of fact, many factors contribute to this glitch phenomenon with the most important one being Bragg diffraction. Prediction of 'energy positions' of glitches based on Bragg's law has been discussed in detail in the previously published papers [24] and the intensity is estimated, in principle, by the kinematical theory. It is however of general / principal interest to investigate beam propagation through lenses also using the dynamical theory of X-ray diffraction. This may serve as a 'reference' for ideal perfect samples in the CRL-context. Theoretical treatments of dynamical diffraction for convex-type samples (like cylinders and

spheres) have been undertaken of, among others, Olekhnovich & Olekhnovich [25]; Saldin [26]; Thorkildsen & Larsen [27], but to our knowledge, works related to concave-type samples are scarce.

However, general / principal interest in such a lens is based on the dynamical theory of X-ray's diffraction. The purpose of this paper is to simulate the intensity distribution for a half lens in the two-beam case for a situation where a conventional X-ray tube is used. Its simulation tool is Mathematica 11.3 [28].

4.3 *Theoretical basis for the experiments using an X-ray lab source*

In general, for those experiments using an X-ray tube as the source, the source-to-sample distance is usually in the order of several tens of centimetres and the source is still considered to be located in the vicinity of the sample's incident surface. Based on this approximation, X-ray lab source is reduced to an ideal point source which emits spherical waves. On top of that, the material of the sample lens is supposed to be high-quality diamond, meaning that the sample lens is treated as a perfect crystal. When these two conditions are satisfied at the same time, it is assumed that the perfect sample is illuminated by a point source. This case, for a slab (semi-infinite) geometry, has been fully investigated by Kato for both absorbing [29] and non-absorbing cases [30].

The total wave in the crystal is obtained by performing the double integration over the so-called "dispersion surface" and expressed as below:

$$\mathbf{D} = \frac{\mathrm{i}}{4\pi} \iint K_{\mathrm{z}}^{-1} \sum_{j} \left\{ \mathbf{D_{oj}} + \mathbf{D_{hj}} \exp[\mathrm{i}\varphi_j(\mathbf{K}, \mathbf{r})] \right\} \mathrm{d}K_{\mathrm{x}} \mathrm{d}K_{\mathrm{y}} \qquad (4.1)$$

where **D** represents the total wavefield inside the crystal, **K** is a wavevector with the magnitude of $k$with its components:

$K_x = K_y = K_z = \sqrt{k^2 - [{K_x}^2 + {K_y}^2]}$, j (j=1, 2) denotes the branches of the two dispersion surfaces and hence should be summed over, $\varphi_j(\mathbf{K}, \mathbf{r}) = -2\pi\left[\mathbf{h}\cdot\mathbf{r} + \mathbf{K}\cdot\mathbf{r_s} + \mathbf{K_{oj}}\cdot(\mathbf{r}-\mathbf{r_s})\right]$, $\mathbf{K_{oj}}$ is the refracted wavevector, $\mathbf{r}$ is the position vector where the wave is investigated and $\mathbf{r_s}$ is the position vector of a point on the crystal surface. The derivation has been given in Authier's work [31].

In order to apply the stationary phase method [32] as shown in Appendix A, the integrand should be pre-manipulated such that it is of the form of the standard integrand. It should also be noted that the incident spherical wave is usually approximated as a cylindrical wave that is normal to the plane of incidence.

By applying the stationary phase method, the reflected amplitude is then written as:

$$D_h = -i\pi\mathcal{B}_h J_0(\varsigma) \tag{4.2}$$

In this equation, $\mathcal{B}_h$ is a proportional factor; $\varsigma = \frac{\pi t}{\Lambda_L}\sqrt{1-\tau^2}$, where t reflects the thickness of the slab, Λ_L is the Pendellösung distance in Laue geometry which can be calculated by the expression:

$$\Lambda_L = \pi V\sqrt{\gamma_0|\gamma_h|}\ /R\lambda C\sqrt{F_h F_{\bar{h}}} \tag{4.3}$$

where γ_0 and γ_h being the cosines of the angles between the normal to the crystal surface and the incident and reflected beams, and the other symbols having usual meanings; τ is used to represent the position of the moving point M (Fig. 30). The abscissa m of a moving point M can be written $\tau = \frac{\overline{EM}}{\overline{EA}}$ and $m = (\tau - 1)\frac{t\cdot\sin 2\theta_B}{2\gamma_h}$. It is important to note that in most geometries that have been dealt with, the path length t is a constant, but for the present case it varies from point to point and is written as:

$$t = \frac{z^2}{2R} + d \tag{4.4}$$

This equation describes a parabolic variation of t with z.

In analogy to the expression for the diffracted amplitude, the refracted amplitude on the side of Borrmann triangle is denoted as:

$$D_0 = -\pi \mathcal{B}_0 \sqrt{\frac{1+\tau}{1-\tau}} J_1(\varsigma) \tag{4.5}$$

where $\mathcal{B}_0$ is the proportional factor for the refracted beam. The intensities for the refracted and diffracted beams are obtained simply by squaring the corresponding amplitude functions.

As is indicated in Fig. 30, the line segments PB and PA represent the refracted and reflected beams, respectively. By connecting the ends of these two lines with a line segment, the closed area intersected by the two beams is referred to as "Borrmann triangle" (△ PAB).

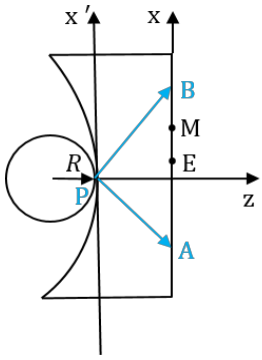

Figure 30 – The Borrmann triangle △ PAB within the half lens is schematically shown and a Cartesian coordinate is also established for the convenience of calculation. Note that PB is the propagation of transmitted beam and PA corresponds to the diffracted beam.

In order to interpret the so-called "Borrmann triangle", it is essential to introduce the Takagi-Taupin equations [33-35] (refer to Subsection 1.4):

$$\frac{\partial D_0(\mathbf{r})}{\partial x_o} = -\mathrm{i}\pi k C \chi_{\bar{h}} D_h(\mathbf{r}) \tag{4.6a}$$

$$\frac{\partial D_h(\mathbf{r})}{\partial x_h} = -\mathrm{i}\pi k C \chi_h D_0(\mathbf{r}) + \mathrm{i} \cdot 2\pi k \beta_h D_h(\mathbf{r}) \qquad (4.6b)$$

In this equation, $D_0(\mathbf{r})$ and $D_h(\mathbf{r})$ represent the amplitudes for the refracted and diffracted beams, $\mathbf{r}$ is the position vector, x_o and x_h represent the unit vectors along the direction of the transmitted and diffracted beams, respectively. C stands for the polarization factor and equals 1 for σ polarization and cos $2\theta_B$ for π polarization with θ_B being the exact Bragg angle, χ_h and $\chi_{\bar{h}}$ are the Fourier coefficients of dielectric susceptibility, β_h is the resonance error describing the deviation from the exact Bragg condition for a specific lattice plane. As can be seen from Eqn. (4.6), T-T equations are constituted by two coupled partial differential equations which describe the wavefields inside the crystal for both deformed and perfect crystals. Generally, T-T equations do not have analytical solutions and they are always solved by using the Riemann-Green method. However, there are two special cases: one is the incident X-ray radiation shining onto a perfect crystal is generated by a spherical source; the other case is the crystal is deformed but with a constant strain gradient. Besides, one should be aware that for perfect crystals, the term $\mathrm{i} \cdot 2\pi k \beta_h D_h(\mathbf{r})$ in Eqn. (4.6 b) can be omitted because β_h can be put to zero after a proper choice of the wavevectors. The equations are reduced to Eqn. (4.7):

$$\frac{\partial D_0(\mathbf{r})}{\partial x_o} = -\mathrm{i}\pi k C \chi_{\bar{h}} D_h(\mathbf{r}); \qquad (4.7a)$$

$$\frac{\partial D_h(\mathbf{r})}{\partial x_h} = -\mathrm{i}\pi k C \chi_h D_0(\mathbf{r}) \qquad (4.7b)$$

In other words, the hyperbolic quasi-linear partial differential equations can be transformed into two ordinary differential equations under specific circumstances. The researcher Sun [36] pointed out that the characteristic lines of these two equations are completely overlapped with the refracted beam (PB) and reflected beam (PA) (*cf.* Fig. 30), and this well explains the formation of the Borrmann triangle in a

mathematical sense. Besides, one should bear in mind that the amplitudes are also obtained by adopting the iterative method discussed in Subsection 11.6.1 (Transmission geometry) by Authier [31].

Due to the rotational symmetry of the "lens geometry", the intensity distribution along the horizontal direction is supposed to follow the same trend as that along the vertical direction. Hence, it is more than sufficient to study the intensity pattern in one direction.

In the case of the slab or flat crystal and the incident X-ray is assumed to be produced by an ideal point source, the simulation results are presented as a reference. When considering the curvature of the entrance surface, we have chosen an approximation approach by replacing the curved surface with several "columns" of different depths. A similar but not equivalent, column approximation is often applied [37]. It has been experimentally verified that a column approximation is a valid approximation in electron transmission microscopy and the prerequisite is that electrons are limited to propagate through the specimen along independent columns and each of these columns are treated as the picture elements of the diffraction contrast image; in other words, the condition should be met that each independent column is so narrow that it will not be interfered even by its neighbouring columns. The column approximation used in electron transmission microscopy has been proven useful when one wants to compute and interpret the images of defects.

Likewise, this approximation may also be extended to the X-ray's case but the width of Borrmann triangle should be small enough and this requires a small Bragg angle. As we know, lower order Bragg reflections excited by relatively higher energy X-rays satisfy the condition and a small Borrmann triangle may thus be anticipated. However, for those high-order Bragg reflections induced by low energy X-ray beams, the approximation is no longer valid because the column is not assumed independent since the constituting columns are likely to be interfered by

other columns. The main reason is a wider Borrmann triangle is spanned. Based on this assumption, we should limit our simulations to the cases of low-order Bragg diffraction (220) and (440) caused by relatively higher energy X-rays. In these cases, each column possibly diffracts X-rays independently and the lateral spread is only associated with the corresponding depth. In the rest of other cases, the curved surface is mimicked by dividing it into separate crystal columns with constant thickness, but they are deemed to be influenced by other columns and the total intensity should be added incoherently. This method is used when one aims to investigate the influence of curvature radius on the refracted intensity.

4.4 *Simulation results and discussions*

4.4.1 Simulations for the flat (slab) crystal as a reference

As derived in the preceding section, an important parameter for the simulation results is the Pendellösung distance (Λ_L) which reflects the periodic exchange of energy between the refracted and diffracted beams and the wavelength of X-ray radiation is set to be 1 Å without loss of generality. Assuming it is a symmetrical Laue transmission case, which means the asymmetry ratio is equal to 0 and the base of Borrmann triangle can be easily computed by the relation: $2t \cdot \tan\theta_{\mathrm{B}} = 25.8\,\mu m$. In this case, (220) Bragg reflection of diamond is chosen as a basis.

To start with, we demonstrate how $J_0(\varsigma)^2$ (solid line) and $J_1(\varsigma)^2$ (dashed line) vary with $\frac{t}{\Lambda_L}$ at the mid-point ($\tau = 0$) of the base AB (Fig. 31) of Borrmann triangle. This reproduces the curves from Authier's work.

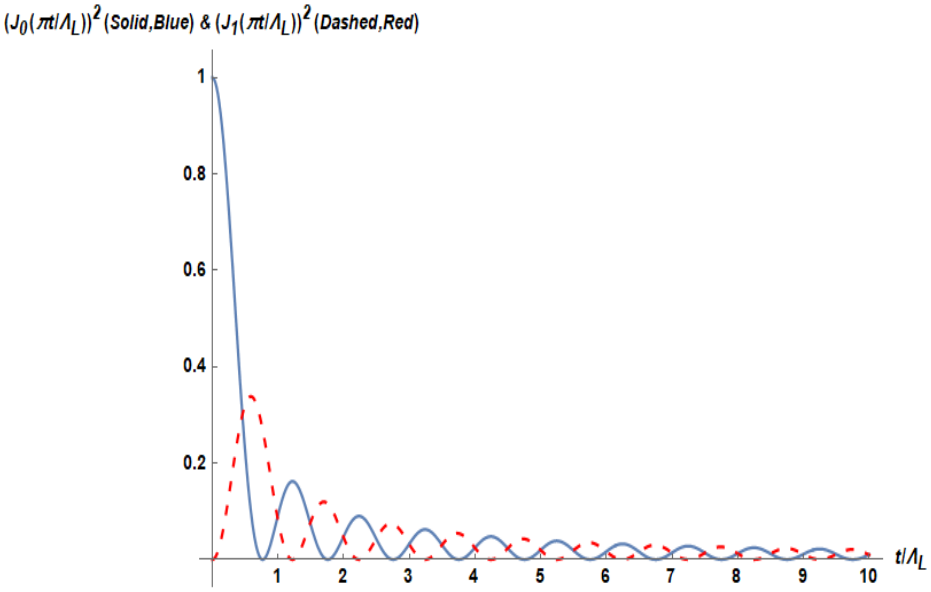

Figure 31 - Variations of $J_0(\varsigma)^2$ (solid line) and $J_1(\varsigma)^2$ (dashed line) with $\frac{t}{\Lambda_L}$ at the center of Borrmann triangle (τ=0) for the slab case. The solid line represents the diffracted or reflected intensity while the dashed line represents the refracted beam.

Neglecting the damping trend, the intensities for the reflected and refracted beams are complementary for a given $\frac{t}{\Lambda_L}$. Moreover, it can be concluded that the period of the oscillation effect is approximately equal to the Pendellösung distance as t/Λ_L is approximately equal to 1. Followed by that, we simulate the flat diamond case with different thickness (*cf.* Fig. 32).

(a)

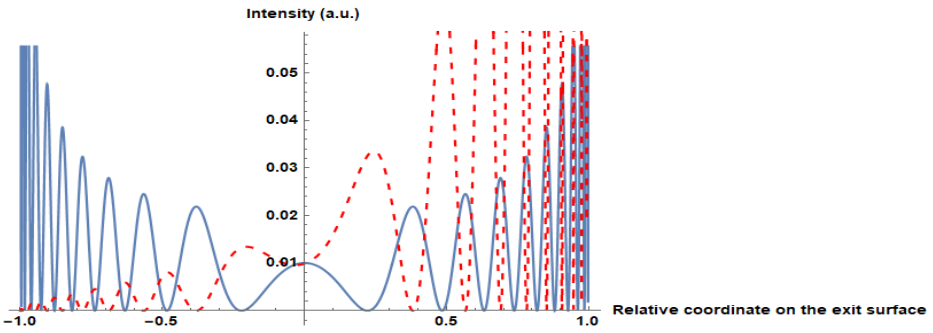

(b)

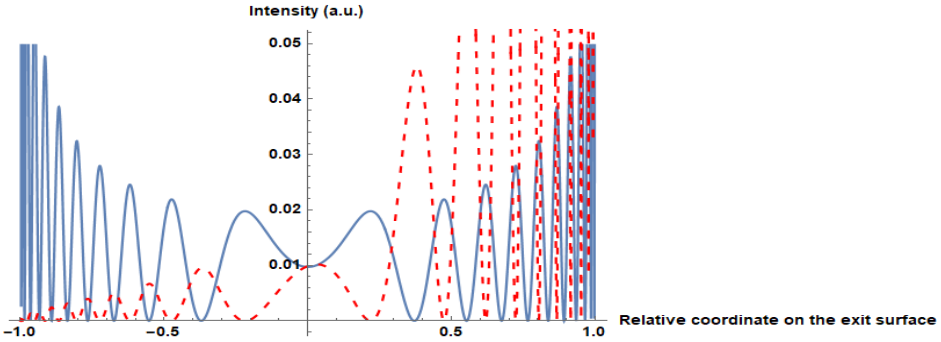

(c)

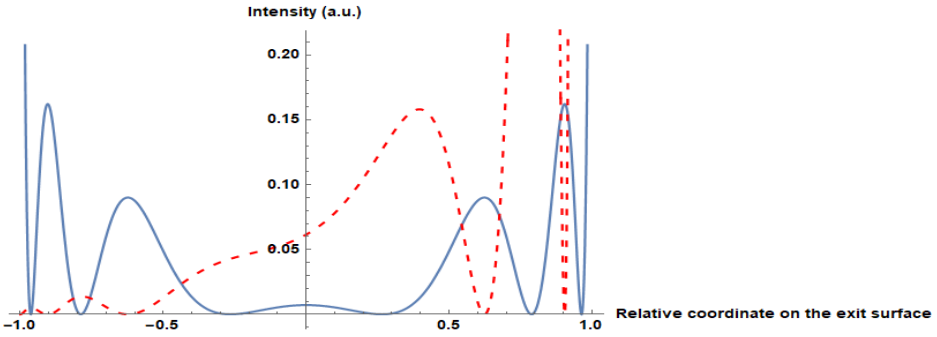

Figure 32 - The intensity distribution on the exit surface of diamond slab for three different cases: $\frac{t}{\Lambda_L}$ is an integer (top); $\frac{t}{\Lambda_L}$ is half integer (middle); t=30 μm in the case of real sample lens (bottom). The horizontal axis denotes the reduced coordinate for a moving point M in Fig. 30. The solid curve represents the diffracted or reflected intensity while the dashed curve represents the refracted beam.

By comparing Fig. 32(a) and 32(b), we come to the conclusion that at the center of Borrmann triangle, the reflected beam reaches its maximum and the refracted beam reaches its minimum if $\frac{t}{\Lambda_L}$ is an integer while it is the opposite trend when $\frac{t}{\Lambda_L}$ is half integer. These simulations retrieve the well-known published results in the textbook [28], for instance, direct comparisons with Fig. 10.4 (a) and Fig. 10.4 (b) in the literature. Besides, all the three figures in Fig. 32 show the same trend that the diffracted and refracted intensities are complementary for every point on the side of Borrmann triangle. On top of that, a "margin effect", that the wavefields are more densely distributed at the edges compared to the central region on the side of the excited Borrmann triangle is also observed and the physical interpretation is given in Appendix B.

In fact, what arouses the researchers' interest is the distribution of the refracted or transmitted intensity on the focal plane. Fig. 33 demonstrates the intensity (a.u.) of the refracted beam when it comes to various classes of Bragg reflections caused by the same X-ray energy or the same reflection but induced by different X-ray energies.

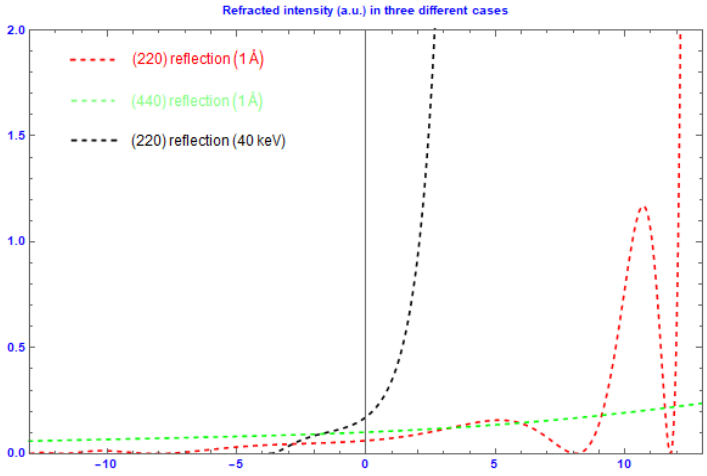

Figure 33 - Three different cases: (220) reflection by X-ray radiation with the wavelength of 1Å, (440) reflection induced by X-ray radiation (1Å) and (220) reflection induced by high energy X-rays (40 keV or 0.31Å) are plotted.

It can be concluded that different combinations of the X-rays' wavelengths and Bragg reflections may yield Borrmann triangles with different areas. By comparing the curves of (220) reflections and its higher order reflection (440) induced by X-rays with the same wavelength, we can find that the lower order reflections give rise to a relatively smaller Borrmann triangle. On top of that, for the same class of reflection, it can be seen that X-rays with a larger wavelength give rise to a Borrmann triangle with a larger area.

4.4.2 Non-interference propagation along each independent columns

Before doing simulations for the 2D half lens, we can start with flat crystals which have a constant thickness. If five point sources are assumed to be aligned along the entrance surface, the intensity pattern is shown in Fig. 34.

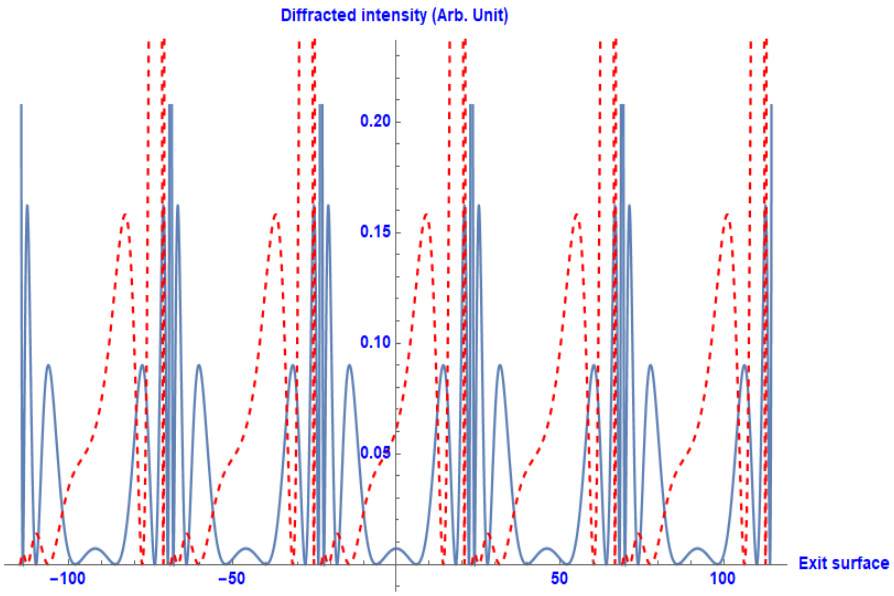

Figure 34 - The intensity patterns in the slab case are simply formed by translating the intensity of one single point source for diamond (220) reflection and the coordinate has been converted from relative coordinate.

The "height distributions" of the columns is calculated based on the "parabolic equation" introduced earlier (Eqn. (4.4)) When the curved entrance surface should be treated seriously, it can be modelled by using staircases with different thicknesses, as is shown in Fig. 35.

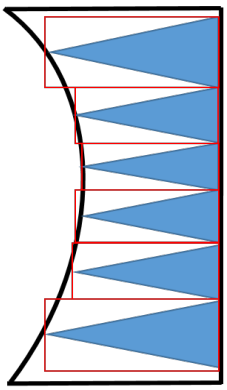

Figure 35 - A sketch of "staircase approximation" to model the concave entrance surface.

By applying the column approximation here, the intensity distribution on the exit surface of the 2D diamond half lens is seen as a repetition of each Borrmann triangle. A minor difference shows when comparing the intensity induced by the source point (the middle one) at the origin and the two point sources located 30 μm from the origin (left and right ones). One can refer to Fig. 36.

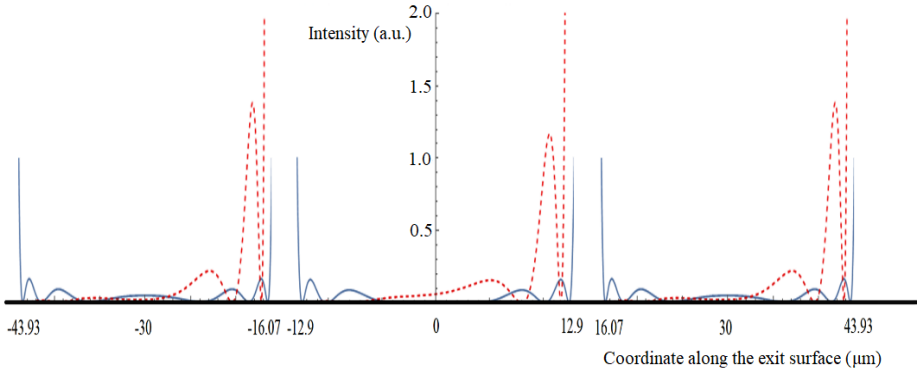

Figure 36 - The intensity distribution along the exit surface of the 2D diamond half lens when each Brorrmann triangle is assumed to propagate independently along its own column.

4.4.3 The influence of curvature radius on the refracted intensity

In some cases, the "columns approximation" is no longer applicable when the included Bragg angle between the refracted and refracted beams is large. In spite of this, we can also deal with curvature by dividing the curved entrance surface into several columns with corresponding thicknesses, and the difference lies in that the columns here are not independent, instead, they can be influenced by other columns. This can be used to study how the curvature radius may affect the refracted intensity.

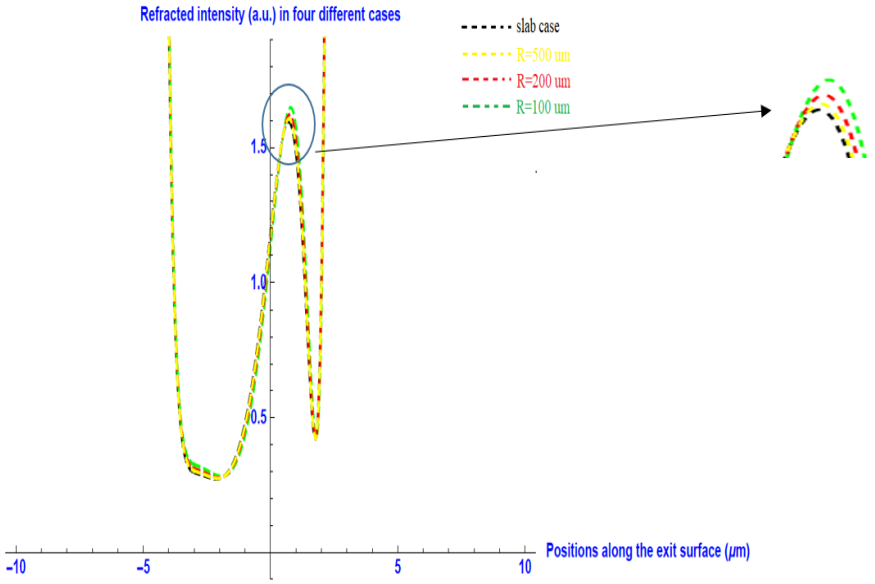

Figure 37 - The refracted intensity along the exit surface for diamond impinged by X-rays at 1Å in four different cases for comparisons: (1) the slab case; (2) the curved entrance surface with the radius of R=500 μm; (3) the curved entrance surface with the radius of R=200 μm; (4) the curved entrance surface with the radius of R=100 μm.

At a first glance of Fig. 37, we can easily come to the conclusion that the intensity distributions for the curved entrance surfaces have higher peaks than the slab case in the central regions of the exit surface by comparing the slab case and three curved cases (treated as a whole set), which

actually demonstrates that a curved concave surface can lead to a better focusing effect. Moreover, all the four curves are almost overlapping and this phenomenon is owing to the fact that the focusing effect of single lens is weak and that is why in real experiments, many lenses are usually stacked together to achieve optimal focusing effect and reasonable focal length. Lastly, it can be inferred from the curves for three curved surfaces with different radii that the smaller the curvature radius is, the sharper the peak will be in the central region of the exit surface. This also complies with previous experimental finding that the radius at the apex of the parabola should be polished down to as small as possible but it is severely limited by currently available etching technique. On top of that, it also shows that by further increasing the radius, the intensity pattern for the curved surface will tend towards that for the slab case and the most extreme case is: provided that the curvature radius is increased to infinity (exactly the slab case), the intensity pattern for the slab case is expected to be retrieved. It is important to note that these simulations are based on non-absorbing crystals and in the case of absorbing crystals, both the Pendellösung distance Λ_L and the Bessel functions should be complex.

4.5 *Conclusions*

This paper studies the case where a Bragg reflection is induced by a point source. This corresponds to those experiments using an X-ray lab source. For the single point source approximation, the amplitudes of the diffracted and refracted beams are proportional to the Bessel function of zeroth order and first order, respectively. This can be derived by taking advantage of the stationary phase method. The simulation results for the flat case show these two beams are always complementary and the intensity patterns are quite sensitive to thickness.

To deal with the concave curvature, the concept of 'column approximation' is introduced and applied in certain circumstances and we are able to replace the curved 2D half lens with several staircases with

different heights. The result shows that the refracted and Bragg reflected beams which constitute the spanned Borrmann triangles propagate along their own columns without getting any interference from the other columns.

Lastly, we primarily focus on the refracted intensity and investigate to what extent the curvature radius may influence the focusing effect. Lower energy X-rays may yield wider Borrmann triangles, which means these divided columns may be affected by neighboring columns and the refracted intensity distribution is thus added incoherently. The simulation result shows that the smaller the curvature radius is, the better focusing effect is obtained. This is in line with real experimental results.

To sum up, this paper investigates the intensity distribution (mainly the refracted intensity) along the exit surface of the 2D half lens in two different cases and the simulations may help the researchers have a better understanding of CRLs, which may lead to further improving their performance. More importantly, this simulation will also provide insight into a more cumbersome case - biconcave CRLs. In addition, one should note that this method is not only limited to CRLs but can also be applied to other X-ray optical devices where Bragg diffraction is expected to appear. However, the limitation of this approximation method is to deal with those experiments using conventional X-ray lab sources and for those having SR as sources will be a subject of future investigation.

4.6 *References*

[1] Weise, H., 2018. The European XFEL—Status and commissioning. CERN Yellow Reports: School Proceedings, 1, p.597.
[2] Shintake, T., 2010. Status report on Japanese XFEL construction project at SPring-8. In Proceedings of the 2010 International Particle Accelerator Conference.
[3] Craievich, A.F., 2019. Synchrotron radiation in Brazil. Past, present and future. Radiation Physics and Chemistry.
[4] Kirkpatrick, P. and Baez, A.V., 1948. Astigmatic X-ray mirrors. J. Opt. Soc. Am, 38, pp.766-774.
[5] Suzuki, Y. and Uchida, F., 1991. X-ray focusing with elliptical Kirkpatrick-Baez mirror system. Japanese journal of applied physics, 30(5R), p.1127.
[6] Liu, W., Ice, G.E., Assoufid, L., Liu, C., Shi, B., Khachatryan, R., Qian, J., Zschack, P., Tischler, J.Z. and Choi, J.Y., 2011. Achromatic nested Kirkpatrick–Baez mirror optics for hard X-ray nanofocusing. Journal of synchrotron radiation, 18(4), pp.575-579.
[7] Erko, A., Agafonov, Y., Panchenko, L.A., Yakshin, A., Chevallier, P., Dhez, P. and Legrand, F., 1994. Elliptical multilayer Bragg-Fresnel lenses with submicron spatial resolution for X-rays. Optics communications, 106(4-6), pp.146-150.
[8] Snigirev, A., 1995. The recent development of Bragg–Fresnel crystal optics. Experiments and applications at the ESRF. Review of scientific instruments, 66(2), pp.2053-2058.
[9] Kumakhov, M.A., 2000. Capillary optics and their use in x-ray analysis. X-Ray Spectrometry: An International Journal, 29(5), pp.343-348.
[10] Dudchik, Y.I. and Kolchevsky, N.N., 1999. A microcapillary lens for X-rays. Nuclear Instruments and Methods in Physics Research Section A: Accelerators, Spectrometers, Detectors and Associated Equipment, 421(1-2), pp.361-364.

[11] Yan, H., Rose, V., Shu, D., Lima, E., Kang, H.C., Conley, R., Liu, C., Jahedi, N., Macrander, A.T., Stephenson, G.B. and Holt, M., 2011. Two dimensional hard x-ray nanofocusing with crossed multilayer Laue lenses. Optics express, 19(16), pp.15069-15076.
[12] Kang, H.C., Maser, J., Stephenson, G.B., Liu, C., Conley, R., Macrander, A.T. and Vogt, S., 2006. Nanometer linear focusing of hard x rays by a multilayer Laue lens. Physical Review Letters, 96(12), p.127401.
[13] Snigirev, A., Kohn, V., Snigireva, I. and Lengeler, B., 1996. A compound refractive lens for focusing high-energy X-rays. Nature, 384(6604), p.49.
[14] Snigirev, A., Kohn, V., Snigireva, I., Souvorov, A. and Lengeler, B., 1998. Focusing high-energy x rays by compound refractive lenses. Applied optics, 37(4), pp.653-662.
[15] Lengeler, B., Schroer, C.G., Richwin, M., Tümmler, J., Drakopoulos, M., Snigirev, A. and Snigireva, I., 1999. A microscope for hard x rays based on parabolic compound refractive lenses. Applied physics letters, 74(26), pp.3924-3926.
[16] Schroer, C.G., Benner, B., Günzler, T.F., Kuhlmann, M., Zimprich, C., Lengeler, B., Rau, C., Weitkamp, T., Snigirev, A., Snigireva, I. and Appenzeller, J., 2002. High resolution imaging and lithography with hard x rays using parabolic compound refractive lenses. Review of scientific instruments, 73(3), pp.1640-1642.
[17] Schroer, C.G., Kuhlmann, M., Lengeler, B., Gunzler, T.F., Kurapova, O., Benner, B., Rau, C., Simionovici, A.S., Snigirev, A.A. and Snigireva, I., 2002, November. Beryllium parabolic refractive x-ray lenses. In Design and Microfabrication of Novel X-Ray Optics (Vol. 4783, pp. 10-18). International Society for Optics and Photonics.
[18] Nazmov, V., Reznikova, E., Snigirev, A., Snigireva, I., DiMichiel, M., Grigoriev, M., Mohr, J., Matthis, B. and Saile, V., 2005. LIGA fabrication of X-ray Nickel lenses. Microsystem technologies, 11(4-5), pp.292-297.

[19] Kononenko, T.V., Ralchenko, V.G., Ashkinazi, E.E., Polikarpov, M., Ershov, P., Kuznetsov, S., Yunkin, V., Snigireva, I. and Konov, V.I., 2016. Fabrication of polycrystalline diamond refractive X-ray lens by femtosecond laser processing. Applied Physics A, 122(3), p.152.
[20] Terentyev, S., Blank, V., Polyakov, S., Zholudev, S., Snigirev, A., Polikarpov, M., Kolodziej, T., Qian, J., Zhou, H. and Shvyd'ko, Y., 2015. Parabolic single-crystal diamond lenses for coherent x-ray imaging. Applied Physics Letters, 107(11), p.111108.
[21] Polikarpov, M., Barannikov, A., Zverev, D., Terentiev, S.A., Polyakov, S.N., Zholudev, S.I., Martyushov, S.Y., Denisov, V.N., Kornilov, N.V., Snigireva, I. and Blank, V.D., 2016, September. Laboratory and synchrotron tests of two-dimensional parabolic x-ray compound refractive lens made of single-crystal diamond. In Advances in Laboratory-based X-Ray Sources, Optics, and Applications V (Vol. 9964, p. 99640J). International Society for Optics and Photonics.
[22] Zholudev, S.I., Terentiev, S.A., Polyakov, S.N., Martyushov, S.Y., Denisov, V.N., Kornilov, N.V., Polikarpov, M.V., Snigirev, A.A., Snigireva, I.I. and Blank, V.D., 2016, August. Imaging by 2D parabolic diamond X-ray compound refractive lens at the laboratory source. In AIP Conference Proceedings (Vol. 1764, No. 1, p. 020006). AIP Publishing LLC.
[23] Polikarpov, M., Snigireva, I., Morse, J., Yunkin, V., Kuznetsov, S. and Snigirev, A., 2015. Large-acceptance diamond planar refractive lenses manufactured by laser cutting. Journal of synchrotron radiation, 22(1), pp.23-28.
[24] Zhang, Q., Polikarpov, M., Klimova, N., Larsen, H.B., Mathiesen, R., Emerich, H., Thorkildsen, G., Snigireva, I. and Snigirev, A., 2019. Investigation ofglitches' in the energy spectrum induced by single-crystal diamond compound X-ray refractive lenses. Journal of synchrotron radiation, 26(1), pp.109-118.
[25] Olekhnovich, N.M. and Olekhnovich, A.I., 1980. Primary extinction for finite crystals. Cylinder. Acta Crystallographica Section

A: Crystal Physics, Diffraction, Theoretical and General Crystallography, 36(1), pp.22-27.
[26] Saldin, D.K., 1982. Bragg diffraction from a material of circular cross section. Acta Crystallographica Section A: Crystal Physics, Diffraction, Theoretical and General Crystallography, 38(4), pp.425-432.
[27] Thorkildsen, Gunnar and Larsen, H.B., 1998. Primary extinction in cylinders and spheres. Acta Crystallographica Section A: Foundations of Crystallography, 54(2), pp.172-185.
[28] Wolfram Research, Inc., Mathematica, Version 11.3, Champaign, IL (2018).
[29] Kato, N., 1961. A theoretical study of pendellösung fringes. II. Detailed discussion based upon a spherical wave theory. Acta Crystallographica, 14(6), pp.627-636.
[30] Kato, N., 1968. Spherical-Wave Theory of Dynamical X-Ray Diffraction for Absorbing Perfect Crystals. I. The Crystal Wave Fields. Journal of Applied Physics, 39(5), pp.2225-2230.
[31] Authier, A., 2004. Dynamical theory of X-ray diffraction (Vol. 11). Oxford University Press on Demand.
[32] Arnol'd, V.I., 1973. Remarks on the stationary phase method and Coxeter numbers. Russian Mathematical Surveys, 28(5), p.19.
[33] Takagi, S., 1962. X-ray dynamical diffraction theory for ideal crystals. Acta cryst, 15, pp.1131-1138.
[34] Takagi, S., 1969. A dynamical theory of diffraction for a distorted crystal. Journal of the Physical Society of Japan, 26(5), pp.1239-1253.
[35] Taupin, D., 1964. Dynamic theory of x-ray diffraction in crystals. Bull Soc Fr Mineral Crystallogr, 87.
[36] SUN, Z.D. and LIANG, J.G., A NEW METHOD OF SOLVING THE TAKAGI EQUATION OF THE DYNAMICAL THEORY OF X-RAY DIFFRACTION.
[37] Howie, A. and Sworn, C.H., 1970. Column approximation effects in high resolution electron microscopy using weak diffracted beams. Philosophical Magazine, 22(178), pp.861-864.

4.7 *Appendices*

Appendix A - Stationary phase method

This method is an approximation method based on Taylor series. Now let us assume to have an integral in the form of

$$I = \int_{-\infty}^{\infty} f(x) \exp[ig(x)]\,\mathrm{d}x$$

First of all, x_0 is assumed to be a root of the first derivative of $g(x)$ and $f(x)$ is a slowly varing function in the neighbourhood of x_0, the integral is then evaluated by expanding $g(x)$ in Talyor series around x_0:

$$g(x) = g(x_0) + g''(x_0)\frac{(x - x_0)^2}{2} + \cdots$$

The integral I is then equal to:

$$I = f(x_0) \exp[ig(x_0)] \int_{-\infty}^{\infty} \exp\left[ig''(x_0)\frac{(x - x_0)^2}{2}\right]\mathrm{d}x$$

Appendix B - Interpretation of "margin effect"

It has been mentioned that the intensity distribution for the Bragg reflected beam reaches its minimum in the central region and increases significantly at both two edges of the Borrmann triangle. As a matter of fact, this phenomenon can be explained by considering that the intensity distribution is a multiplication of density of wavefields and diffracted or reflected power. For example, the wavefields reaching the base of Borrmann triangle close to the triangle apex B ($\tau = -1$), the reflecting power is small but on the contrary, the density of the wavefields is large, leading to a densed intensity distribution; However, when it comes to the center of Borrmann triangle ($\tau = 0$), the density of wavefields is the sparsest and so is the intensity distribution; Similarly, at the other edge of the Borrmann triangle, the triangle apex C ($\tau = +1$), intensities for the refracted beam are also very small, but due to the large density of wavelfields, the intensity distribution is also very large.